Role of the Early Miocene Jinhe-Qinghe Thrust Belt in the building of the Southeastern Tibetan Plateau topography

Chengyu Zhu[1], Guocan Wang[1,2], Philippe Hervé Leloup[3], Kai Cao[1,2], Gweltaz Mahéo[3], Yue Chen[1], Pan Zhang[1], Tianyi Shen[1], Guiling Wu[1], Paul Sotiriou[4], Bo Wu[1]

1 Center for Global Tectonics, School of Earth Sciences, China University of Geosciences, Wuhan, China.

2 State Key Laboratory of Geological Processes and Mineral Resources, China University of Geosciences, Wuhan, China.

3 Laboratoire de Géologie de Lyon: Terre, Planètes et Environnement, Université Claude Bernard, Villeurbanne, France.

4 School of the Environment, University of Windsor, Windsor, ON N9B 3P4, Canada.

Corresponding author: Guocan Wang (wgcan@cug.edu.cn**)**

Key Points:

- The Baishagou granite experienced 1.5-2.2 km of exhumation at a rate of 0.42 km/Myr at ~20-15 Ma.
- The thrusting along thrust belts are responsible for relief generation during Oligocene to early Miocene in southeast Tibet.
- Cenozoic exhumation/relief creation history in southeast Tibet cannot be explained by a single mechanism, at least three phases are recorded.

Abstract

Understanding the development of key thrust faults in southeastern Tibet is significant to reconstructing the geodynamic and topographic processes. Detailed structure analysis along the ~400 km long Jinhe-Qinghe thrust belt (JQTB) indicate thrust motion with a minor left-lateral component. The exhumation history of the Baishagou granite, based on apatite (U-Th)/He and fission-track thermochronology and thermal modeling, suggest an accelerated exhumation rate (~0.42 km/Myr) between 20 and 15 Ma. We interpret that fast exhumation due to the activation of the Nibi thrust, a northern branch of the JQTB. The ~1.5-2.2 km of exhumation that occurred corresponds to the present topographic difference across the thrust belt. In the Early Miocene, significant relief along JQTB was generated by thrusting. When compared with previous studies it appears that Cenozoic exhumation and relief creation in southeastern Tibet cannot be explained by a single mechanism. Rather, at least three stages of relief creation should be invoked. The first phase is an Eocene NE-SW compression partly coeval with Eocene sedimentation. During the Late Oligocene to Early Miocene the second thrusting phase occurred along the Yulong and Longmenshan thrust belts, and then migrated to the JQTB further to the southeast during 20-15 Ma. A third phase involved the activation of the Xianshuihe fault and the re-activation of the Longmenshan thrust belts and the Muli thrust. The interaction between thrusting and fast river erosion triggered by climate change is not certain but thrusting along thrust belts appears to explain most of the present-day relief in the southeastern Tibetan Plateau.

Plain Language Summary

Understanding the development of the principal thrust fault in southeastern Tibet can help to reconstruct the geodynamic and topographic evolution. In this paper, detailed field structure observations along the Jinhe-Qinghe thrust belt (JQTB), which is considered as a part of the Yalong thrust belt, indicate thrust motion with a minor left-lateral component. Besides, apatite (U-Th)/He and fission track thermochronology and thermal modeling are applied to reconstructing the cooling and exhumation history of the Baishagou granite, which is in the hanging wall of the Nibi fault, a branch of the JQTB. Our results show the Baishagou granite experienced rapid exhumation at ~20–15 Ma at a rate of ~0.42 km/Myr, corresponding to the present topographic difference across the thrust belt. Combined with previous studies in southeastern Tibet, we propose the differential exhumation resulted from thrusting along thrust belts are responsible for relief generation during Oligocene to early Miocene. Furthermore, it appears that at least three stages of Cenozoic shortening, and relief creation are documented by

different kinds of studies (e.g., paleo-altimetry, low-temperature thermochronology, sedimentology). That is, Cenozoic exhumation and relief creation in southeastern Tibet does not follow a simple pattern that could be explained by a single mechanism.

1 Introduction

The Tibetan Plateau, the largest orogenic plateau on earth, results from complex crustal deformation processes in the context of ongoing collision and indentation of the Indian and Asian continents that commenced at least ca. 60-50 Ma ago (Molnar & Tapponnier et al., 1975; Tapponnier et al., 2001; Hu et al., 2016). Many geodynamic models have been proposed to explain the growth and expansion of the southeastern Tibet plateau. For example, the block lateral extrusion model proposed rigid block escape along the major boundary strike-slip faults, and as a consequence, the crustal shortening and thickening are widely distributed on the margins of the plateau (Tapponnier et al., 2001). Another model proposes that the crust thickened by a lower crustal flow which propagates from interior Tibet toward the southeastern margin. Consequently, the present continuous and gentle topography was generated in southeastern Tibet in the Middle Miocene (Royden et al., 1997; Clark et al., 2005). Southeastern Tibet is a key area to quantify the on-going process of plateau migration and topography evolution because of the presence of upper crustal shortening structure as well as elevated low-relief topography deeply dissected by large rivers as a result of regional uplift and subsequent incision (Burchfiel et al., 1995; Tian et al., 2012; Clark et al., 2005a; Liu-Zeng et al., 2008; Yang et al., 2016).

The recent GPS velocity field (Zhang et al., 2004) confirmed that the plateau material migrates from the interior of Tibetan Plateau to the eastern and southeastern margin. Several studies targeted at the boundary strike-slip faults between different blocks (e.g., Leloup et al., 1995, 2001; Replumaz et al., 2001; Xu and Kamp, 2000; Zhang et al., 2017; Wang et al., 2017). Many other studies have been published on the Longmenshan (LMS) thrust belt. Only a few scattered thermochronology data have been reported from the Yalong margin in the southwest prolongation of the LMS (Figure 1), where thrust faults have been reported (S. Wang et al., 2012; Wu et al., 2019). Most studies suggest that these thrust faults are minor and that the main Miocene thickening process is channel flow (e.g., Clark et al., 2005). Structural evidence of the thrust faults is still lacking, and plays a vital role in thermochronology data interpretation. Understanding the geometry and kinematics of these large-scale thrust faults, as well as thrust-induced exhumation pattern, is crucial for deciphering the mechanism of extension and the geomorphic evolution of the Tibetan Plateau.

In this paper, we re-asses the Jinhe-Qinghe thrust belt along the Yalong margin through the utilization of detailed field structure analysis. Furthermore, an age (apatite fission track (AFT) and apatite (U-Th)/He (AHe))-elevation profile collected from the Jurassic Baishagou granite located at the hanging wall of the Nibi thrust, a northern branch of the Jinhe-Qinghe thrust belt, will facilitate reconstructing of its cooling history. This age data will provide a time constraint on the activation of the Jinhe-Qinghe thrust belt. The Oligocene-Miocene structural and relief evolution of southeastern Tibet will be discussed in light of this new age data.

2 Geological setting

The Cenozoic tectonics of southeastern Tibet is marked by several large-scale strike-slip faults including the Xianshuihe, Ailao Shan-Red River and Litang faults (Figure 1) (Allen et al., 1991; Leloup et al., 1995; Zhang et al., 2015). North of the left-lateral Xianshuihe fault, a protracted history of mountain building from the Upper Triassic to the present day, has been documented in the NE-SW trending LMS thrust belt (Burchfiel et al., 1995; Roger et al., 2004; E. Wang et al., 2012; Tian et al., 2013). This thrust belt is located at the sharp topographic transition from the Tibetan Plateau to the Sichuan Basin. South of the Xianshuihe fault the topographic transition is less sharp but remains steep with the average elevation dropping from ~4200 m to ~1800 m over a distance of 200-250 km (Liu-Zeng et al., 2008). Few detailed studies have focused on the thrust faults in this area, however, NE-SW-trending faults (e.g., Jiulong, Muli, Yulong, Jinhe-Qinghe faults) with apparent reverse motion appear on large-scale geological maps (Figure 1) (Burchfiel et al., 1995; Wang et al., 2012; Perrineau, 2010; Cao et al., 2019). The Muli and Jinhe-Qinghe faults have been designated as the Yalong thrust belt and interpreted as the southward continuation of the LMS thrust belt (Figure 1) (e.g., Burchfiel et al., 1995; Clark et al., 2005; S. Wang et al., 2012; Cao et al., 2019). The faults merge together before branching on the left-lateral Xianshuihe fault, with a ca. 60 km offset. The absence of any flexural basin and the relative smoothness of the relief drop with respect to that of the LMS led to the hypothesis that the present-day topography mostly resulted from passive uplift above a lower crustal channel flow that originated below central Tibet and veers around southern Sichuan, rather than from thickening along the Yalong thrust belt (Clark et al., 2005). This uplift would have warped up a low-relief erosion surface originally formed at low elevation, and induced entrenchment of the major rivers. Low-temperature thermochronology suggests that this entrenchment started at ~13-9 Ma, giving a proxy for the timing of surface uplift (Clark et al., 2005; Ouimet et al., 2010). However, other studies document that other rivers in southeastern Tibet underwent entrenchment from the Oligocene to early Miocene (30-20 Ma)

(Shen et al., 2016; Tian et al., 2014). Detailed topographic studies indicate that the mean elevation drops abruptly across the Muli thrust and JQTB (Liu-zeng et al., 2008; Wu et al., 2019). Based on field observations and geological cross-sections, Perrineau (2010) estimated that ~12.5 km and ≥22.5 km of horizontal shortening occurred across the JQTB and Muli fault, respectively, with ~3.5 km of hanging wall uplift in both cases. Both the Yangtze and Yalong rivers exhibit large bends when crossing the Yulong and Muli thrusts, respectively (Figure 1). Near the Yalong bend, S. Wang et al. (2012) interpret the Jinhe-Qinghe fault as a thrust fault with a left-lateral component branching on the Xianshuihe fault. Moreover, S. Wang et al. (2012) deduced from the age versus elevation relationship of ten apatite fission track ages (AFT) that an increase in the apparent cooling rate beginning at ~17 Ma was indicative of the onset of the fault. The AFT samples appear to have been collected on the Jinhe-Qinghe fault footwall rather than the hanging wall over a large horizontal distance of about 80 km (Figure 2), however, rendering this constraint on the timing of fault onset unconvincing.

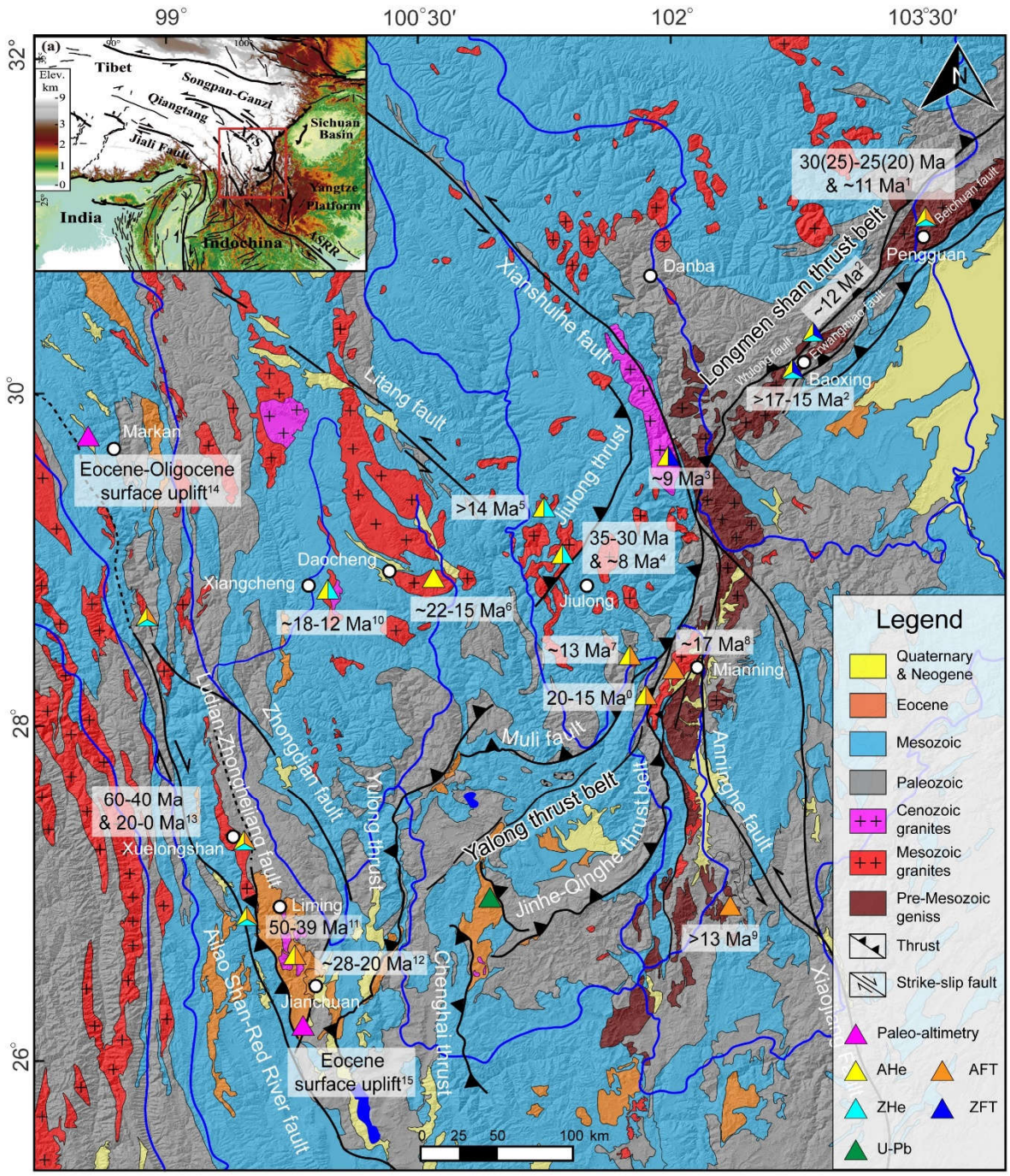

Fig. 1. Simplified geology and topography of southeastern Tibet, with major faults (modified after Leloup et al., 1995; Zhang et al.,2017; Cao et al., 2019). The inset in the upper left corner shows the location of southeastern Tibet. The triangle symbols denote accelerated exhumation phases derived from low-temperature thermochronology in southeastern Tibet: 0 = This study, 1 = E. Wang et al. (2012), 2 = Cook et al. (2013), 3 = Zhang et al. (2017), 4 = Zhang et al. (2016), 5 = Ouimet et al. (2010), 6 = Tian et al. (2014), 7 = Clark et al. (2005), 8 = S. Wang et al. (2012), 9 = Wang et al. (2017), 10 = Gourbet et al. (2020), 11 = Cao et al. (2020), 12 = Cao et al. (2019), 13 = Liu et al. (2018), 14 = Su et al. (2018), 15 = Hoke et al. (2014).

3 Structural observations along the Jinhe-Qinghe Thrust Belt

As described above, the Jinhe-Qinghe fault begins to branch progressively away from the Muli fault from 28°40'N southwards (Figure 1, Figure 2). The Jinhe-Qinghe fault is split into several branches (see below), accordingly, we would like to redefine it as the Jinhe-Qinghe thrust belt (JQTB), rather than the Jinhe-Qinghe fault (S. Wang, et al., 2012). The main fault stretches from north of Mianning city to the Yongsheng area, east of the Chenghai thrust fault (Figure 1, Figure 2). Detailed structural analysis from six different sites along the JQTB is presented below.

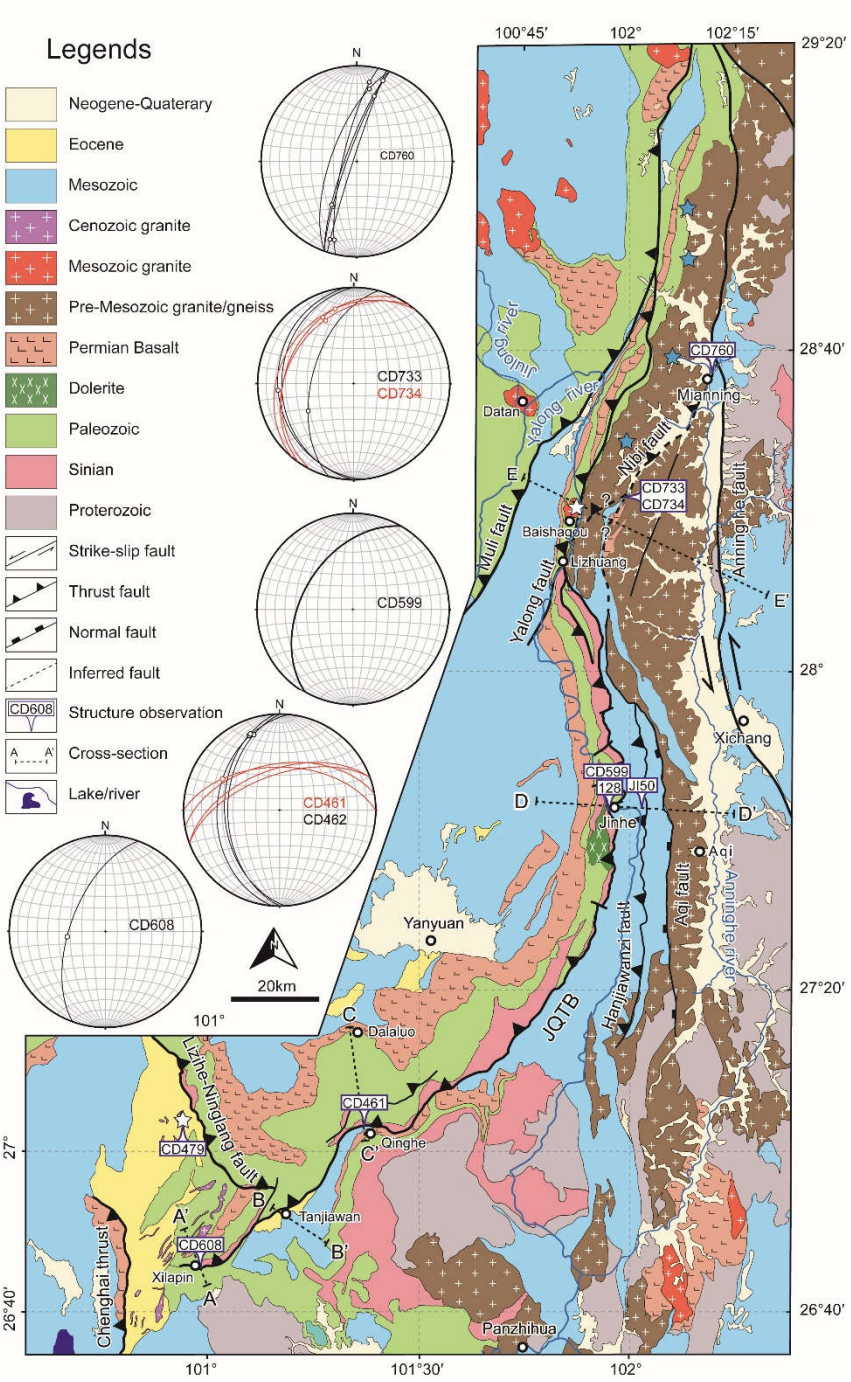

Fig. 2. Geological map of the Jinhe-Qinghe Thrust Belt based on BGMR Yunnan (1990), BGMR Sichuan (1991), S. Wang et al. (2012), and our new field observations. Stereoplots are shown of the Jinhe-Qinghe thrust belt at sites CD608, CD461 and CD462, CD508, CD733 and CD734, CD760, and CD759, from south to north, respectively. The locations of cross-sections A-A', B-B', C-C', D-D', E-E', and corresponding outcrops pictures are provided in Figures 3-7. The blue star denotes the AFT samples' locations in S. Wang et al. (2012). The white stars denote the sample locations in this study.

3.1 Xilaping cross-section

This area is located near the western end of the main Jinhe-Qinghe fault, about 20 km to the east of the Cheng Hai thrust. At site CD608 (Figure 2), a fault damage zone with unconsolidated fault breccias and cataclastics, separates Sinian dolomite from Devonian siltstone (Figure 3a) (Geol. map G47-11). The fault strikes NE-SW and dips 60-70° NW, to the northwest with an apparent reverse motion (Figure 3b and 3h). The Sinian dolomite is affected by several faults (Figure 3c), with the main fault plane showing nearly downdip slickensides with crystallization steps suggesting a thrust motion with a minor left strike-slip component (Figure 3d, e and 3i). In the damage zone, ill-deformed dolomite lenses are surrounded by schistose levels. The lenses' sigmoidal shapes are compatible with reverse motion in the fault zone (Figure 3c, 3f and 3g).

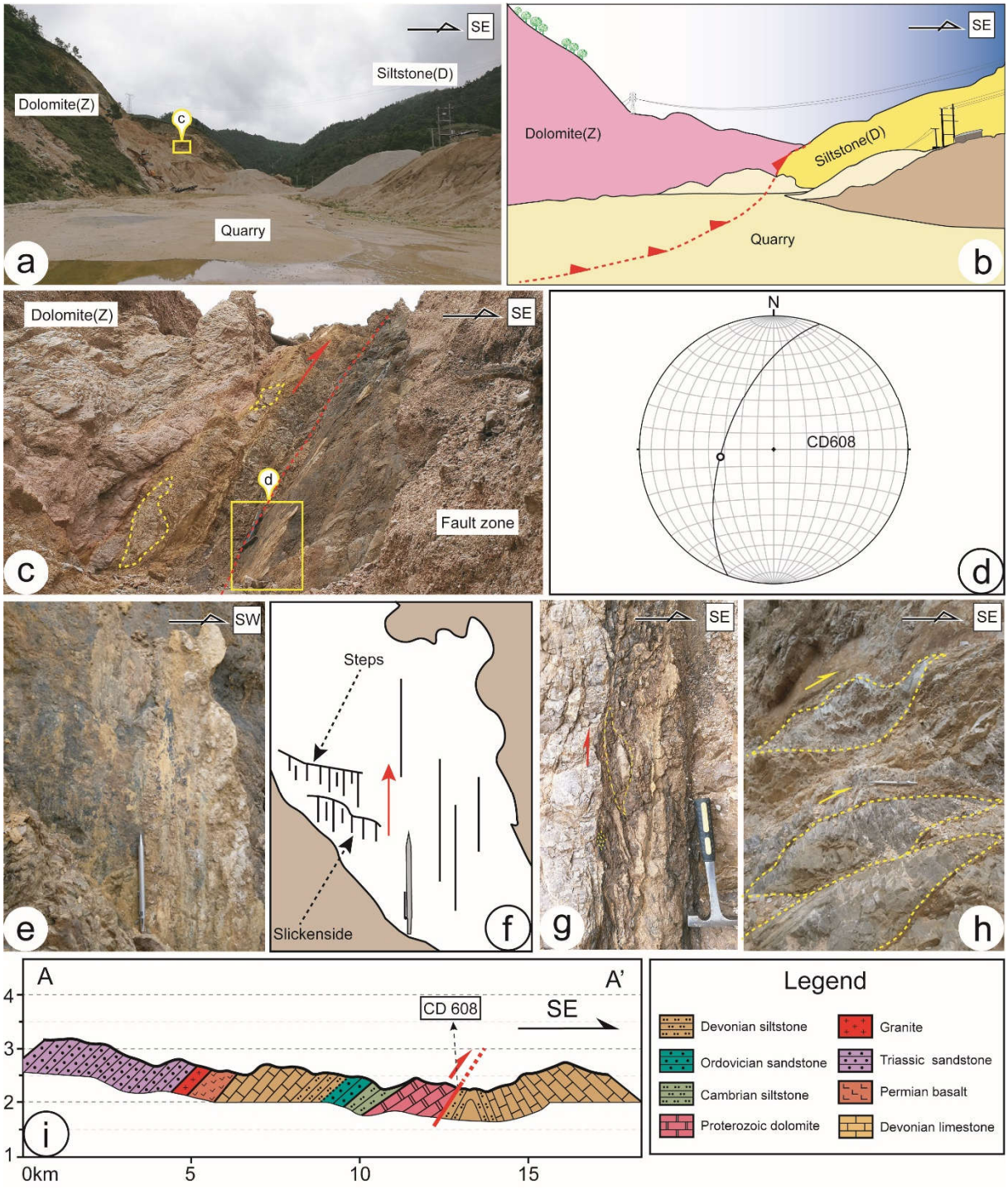

Fig. 3 Field observations in the Xilaping area. (a) Site CD608 picture with Sinian (Z) dolomite on the left and Devonian (D) sediments on the right. (b) Sketch corresponding to Figure 3a. (c) Damage zone in the dolomite. (d) Stereo plot (lower hemisphere) of the main fault plane and slickenside. (e) Close up of the fault plane with slickensides indicating thrust motion (see location in Figure 3c). (f) Sketch corresponding to Figure 3e. (g) and (h) Asymmetric dolomitic lenses compatible with the reverse motion of the JQTB. (i) Cross-section in the Xilaping area

perpendicular to the strike of the fault. See Figure 2 for the location. Vertical exaggeration is 2x.

3.2 Tanjiawan cross-section

According to the published geological maps in the Tanjiawan area, the JQTB separates gray Devonian limestone (D_2-D_3) from the siliciclastic rocks of the Eocene Hongyazi Fm. (Eh) (Figure 2) (Geol. map G47-12; S. Wang et al., 2012). Further northeast and to the south of the Yanyuan, the Hongyazi Fm.is though to be Late Eocene in age, according to mammal, plant and Ostracoda fossils (Si et al., 2000). This observation is important as it implies that the JQTB fault is younger than Late Eocene in age. The Hongyazi Fm. is composed of conglomerates with limestone clasts at the bottom (Figure 4d) and purple/red fine-grained sandstone and siltstone in the upper part (Geol. map G47-12). The Hongyazi Fm. dips to the NW (Figure 4b) and unconformably overlap a Late Jurassic coal-bearing formation (Figure 4e). The precise geometry of the JQTB is obscured because of heavy vegetation (Figure 4a-c), however, it is likely a NE-SW fault that dips steeply to the NW. A cross-section indicates a vertical offset of ~4 km (Figure 4e).

North of the Tianjiawan basin, the geological maps show an NW-SE fault placing Sinian dolomite and Paleozoic sediments on top of the Eocene rocks of the Ninglang basin (Figure 2) (Geol. map G47-11; Gao et al., 2017). The fault is called the Lizihe-Ninglang fault (LNF) (S. Wang et al., 2012), and the Eocene sediments belong to the Ninglang Fm (En), which is quite similar to the Hongyazi Fm. S. Wang et al. (2012) inferred the sediments to be Oligocene to Miocene in age. However, they are intruded by a series of granitic bodies (Figure 2, 4f) (Geol. map G47-11), one of which has been dated at 33.1 ± 0.2 Ma (Early Oligocene) by zircon U-Pb geochronology (Figure 4f, 4g; Table S1). This age confirms that the Ninglang Fm. is older than Early Oligocene, and may have a similar age to the Hongyazi Fm., implying that the LNF initiated after the Late Eocene-Early Oligocene. To the south, the LNF appears to be cut by a branch of the JQTB (Figure 2) suggesting LNF could be older rather than a branch of JQTB.

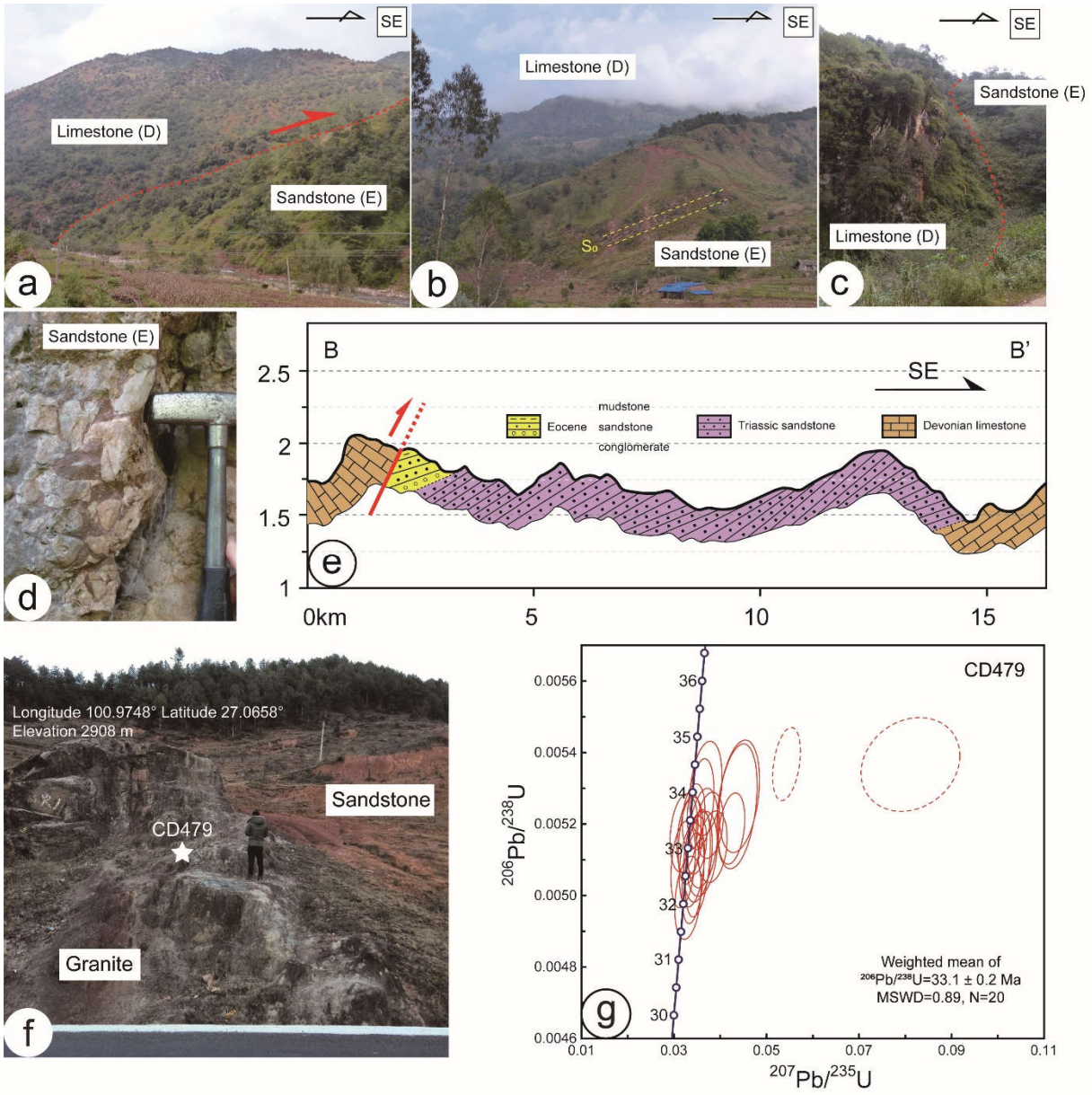

Fig. 4 Field observations in Tanjiawan and Ninglang. (a)-(d) Outcrops in the Tanjiawan Eocene Basin. (d) Conglomerates with limestone pebbles at the bottom of the Hongyazi Fm. (e) Cross-section across the Tanjiawan Eocene basin. See Figure 2 for the location. Vertical exaggeration is 3x. (f) Picture of site CD479 where granite is intrusive into sediments (Ninglang Fm.). (g) Concordia plot of Zircon U-Pb data of the granite intrusion shown in (f) (sample CD479).

3.3 Qinghe-Dalaluo cross-section

The middle segment of the JQTB is exposed on the road from Panzhihua to Yanyuan (section C-C', Figure 2). In this area, the thrust belt comprises two branches with the southern one being the primary fault. According to the geological map, the southern fault branch is itself composed of two splays, the lower, southern one trending N90° and bringing Sinian rocks on top of

Permain-Triassic rocks (Geol. map G47-12) with a vertical offset of ca. 1 km. Our observations at site CD 461 show a large fault plane striking N80° and dipping ~50° NNW that bears slickensides trending N298° (red planes in Figure 5c). According to the geological map, the northern branch of the JQTB strikes N60° and brings Devonian sediments on top of folded Carboniferous limestone with a vertical offset of ~500 m (Figure 5c) (Geol. map G47-12). At site CD462, the bedrock is highly fractured, and a series of subparallel secondary reverse faults form an imbrication zone with roof and floor thrusts bounding a dolomite fragment and forming a duplex structure (Figure 5a). This geometry suggests a top to the east thrust motion (black planes in Figure 5c). A large fault plane strikes N5° 35° and bears slickensides trending N338° with steps suggesting left-lateral (with minor thrust) motion (Figure 5b).

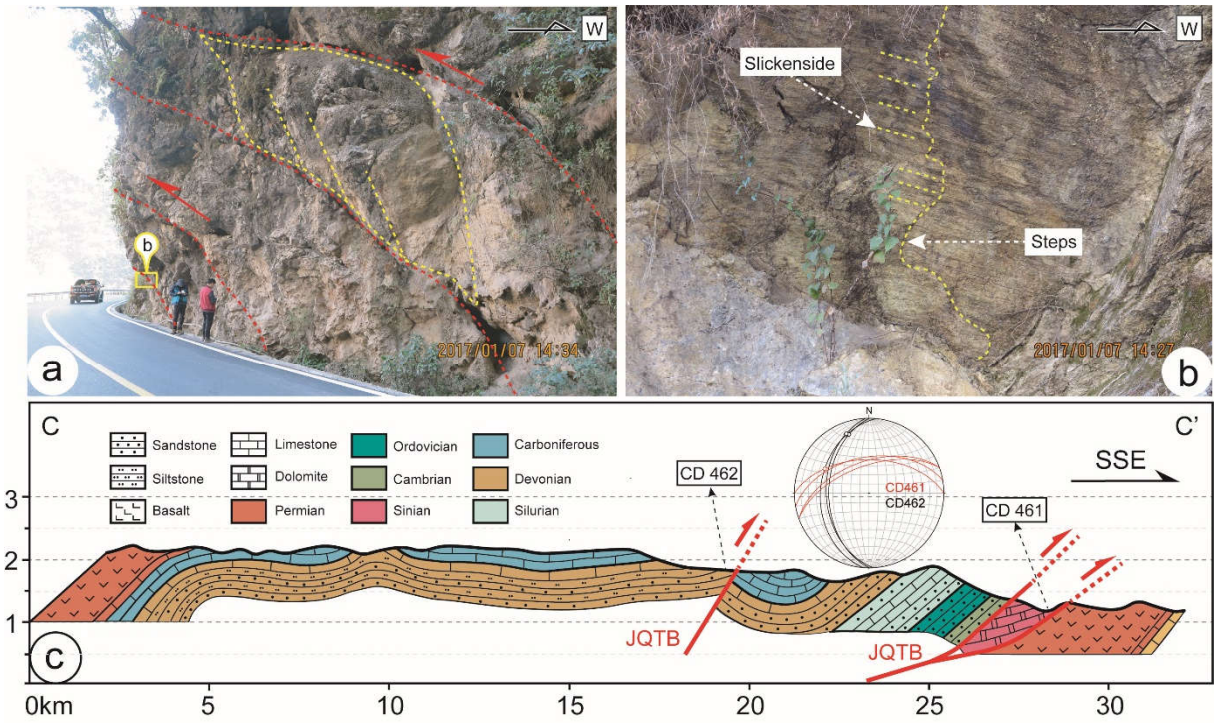

Fig. 5 Field observations along the Qinghe-Dalaluo cross-section. (a) Outcrop of a series of minor faults at site CD462. (b) Slickensides and steps developed in the Devonian limestone (inset shown in (a)). (c) Qinghe-Dalaluo cross-section. See Figure 2 for the location. Vertical exaggeration is 2x.

3.4 Jinhe cross-section

East of 100°30'E the strike of the JQTB veers from NE-SW to N-S (Figure 2) (Geol. map G47-06). The JQTB can be continuously traced for more than 100 km from site CD461 of the Qinghe-Dalaluo section until site 128, near the Jinhe town, where the fault strikes N60° 65°N and places Sinian rocks (gabbros and Sinian limestones) over Upper Permian basalts (Figure 6f, 6d). The fault zone is complex with several parallel fault traces. Most faults dip steeply to

the W, but locally Devonian limestone is thrust over Triassic-Jurassic siltstone along a flatter surface (Geol. map G47-06) (Figure 6f). To the west, at site CD599, a fault strikes N30° 45°W with the hanging wall comprising Sinian and Paleozoic rocks, while drag folds are found adjacent to the fault zone implying a thrusting movement (Figure 6a-c). From a cross-section (Figure 6f), the vertical component of motion on the JQTB can be estimated at ~1.8 km.

East of the JQTB, Late Triassic siltstone with interbedded coal beds and Jurassic siltstone are strongly folded by a series of anticlines and synclines with axes subparallel to steeply-dipping N-S reverse faults, the most prominent one being the Hanjiawanzi fault that brings Triassic rocks on top of Jurassic rocks (Figure 6f). Further east, Mesozoic sediments are separated from the Aqi batholith by a west-dipping fault with an apparent normal throw that we term the Aqi fault (Figure 6f) (Geol. map G48-01). Despite its apparent throw, that fault has been interpreted as a major thrust extending for more than 300 km (Figure 2). Both the Hanjiawanzi and Aqi faults extend further to the south (Figure 2).

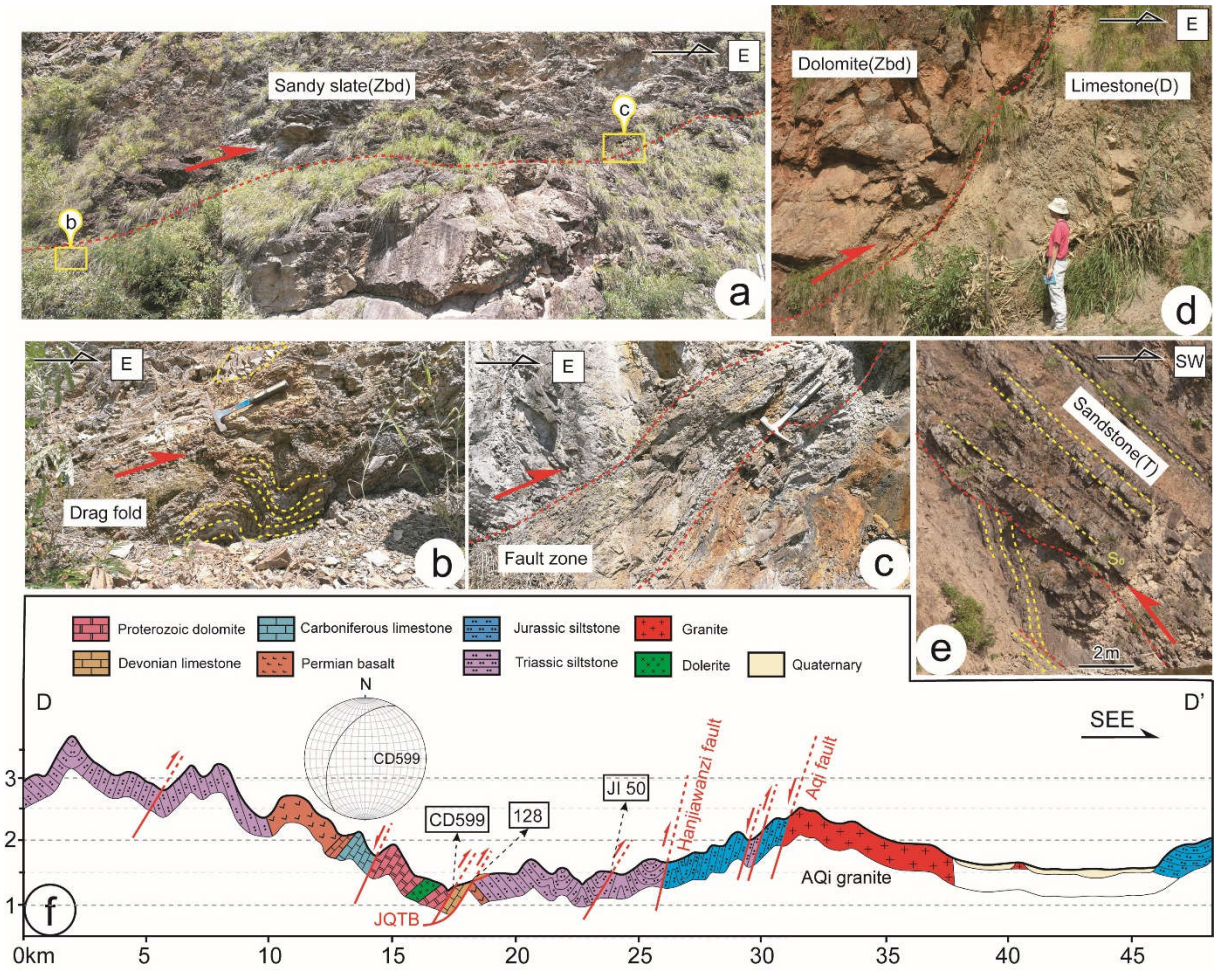

Fig. 6 Field observations along the Jinhe cross-section. (a)-(c) Outcrops of the fault zone and drag fault in Sinian dolomite near the Jinhe bridge (site CD599). (d) site 128. Outcrop of Sinian

(Zbd and gabbros) above Upper Permian basalts. (e) Thrust fault within Triassic siltstones at site JI50. (f) Jinhe cross-section. See Figure 2 for the location. Vertical exaggeration is 2x.

3.5 Mianning–Yalong cross-section

North of the Jinhe cross-section the JQTB can be followed to the NNW to the Lizhuang area, bringing Sinian rocks (Zbd) above Mesozoic sediments (Figure 2) (Geol. map G47-06). Near Lizhuang, the JQTB and the Yalong fault branch together before turning to the NNE and becoming progressively more linear closer to the Muli thrust (Figure.2). The kinematics of the Yalong fault is thrust with a sinistral component which has been interpreted as a branch of the JQTB (S. Wang et al., 2012).

Sites CD733, CD733b and CD734 show evidences for ~N-S faulting. At site CD733, fault gouge in the granite exhibits fault planes and slickensides, and steps that are indicative of thrusting motion (Figure 2; 7a-b). Approximately 500 m away, site CD733b shows cataclastic granite is thrusted over Triassic sandy slate (Figure 7c). The grey slate is strongly schistose parallel to a fault plane striking N15° 54°N with slickensides trending N339° and shear criteria suggesting thrust motion (Figure 2, Figure 7d). At site CD734, a contact surface brings Triassic sandy slate on top of Triassic carbonaceous slate (Figure 7e). The contact plane show undulations and strikes ~N30° and dips 25-35°W (Figure 2). S-C fabrics and asymmetric lens in the fault zone suggest left-lateral thrust motion (Figure 7e). These three observation sites occur along the Nibi fault mapped ~8 km east of the Yalong fault (figure 2) (Geol. map H47-36). To the south, the Nibi fault possibly extends to the Lizhuang area (S. Wang et al., 2012), as a branch of the JQTB. It is unlikely that the Nibi fault connects with the Aqi fault, which is a normal fault in the south parallel to the JQTB (Geol. map G47-06), while to the north its trace is obscured by Quaternary sediments.

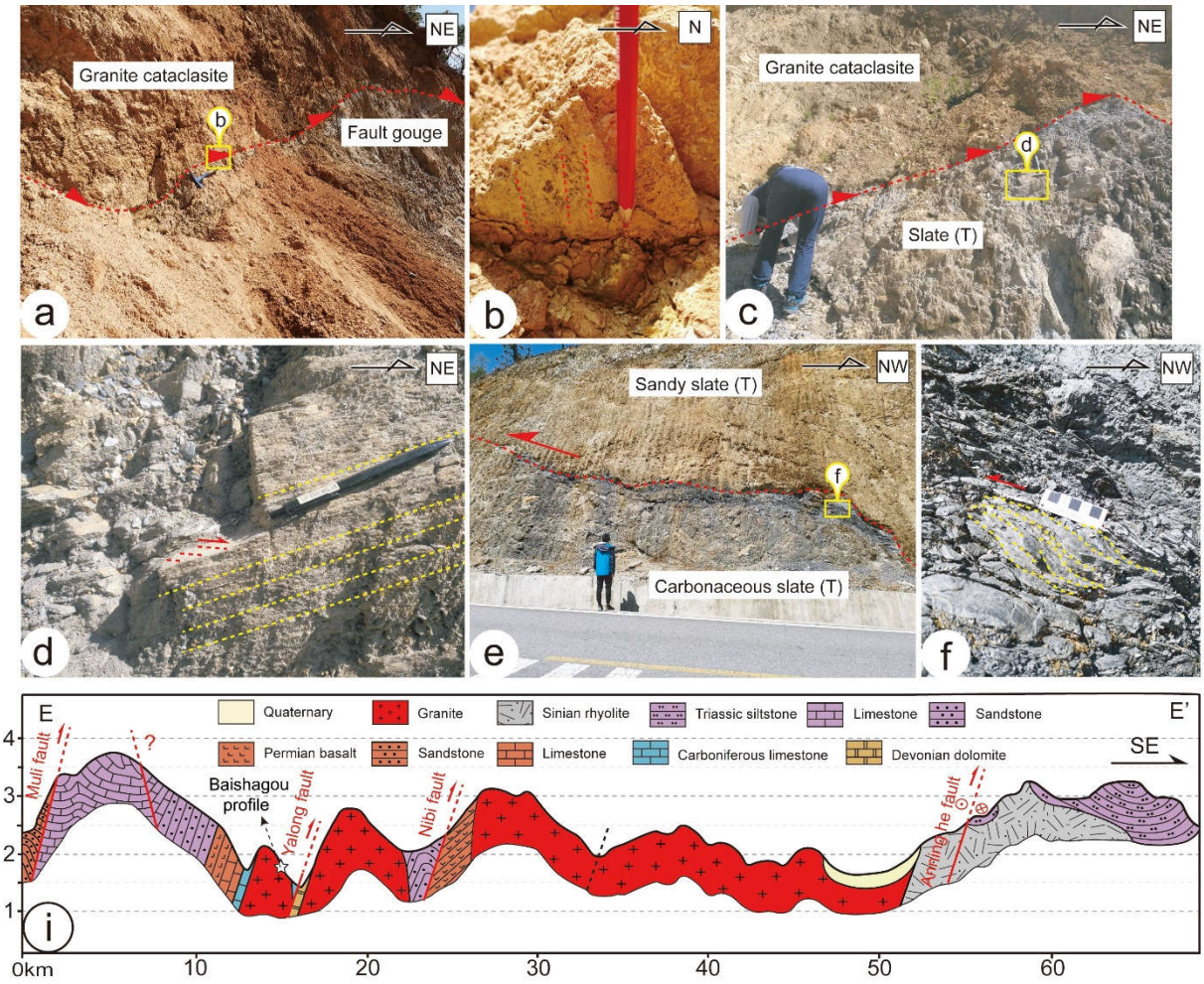

Fig. 7 Field observations along the Mianning–Yalong section. (a-b) site CD733. Cataclastic granite. (b) Fault plane striking N355° 52°W with slickensides trending N339°. (c-d) Site CD733b showing thrusting of granite on top of Triassic slate. (d) Triassic sediments are strongly schistosed with slickenside trending N335°. (e-f) CD734 Outcrop of the contact between sandy slate and carbonaceous slate at the site. (f) S-C fabrics in carbonaceous slate near the structure contact. (i) Mianning-Yalong cross-section. See Figure 2 for the location. Vertical exaggeration is 3x.

At site CD760, west of the left-lateral Anning He fault, a fault striking N50° separates Sinian granites and Permian basalts (Figure 2) (Geol. map H48-31). Although the contact relationship is unclear due to heavy vegetation, the granites and the Permian metamorphic basalts are deformed and cataclastic near the contact (Figure 8b). Fault planes found in the basalt are nearly vertical, strike ~N20° and show two groups of slickensides: one trending N15° and the other one trending N210°. The former one shows left-lateral with minor thrust motion, while the latter

one shows left-lateral motion with a minor normal component (Figure 2). In the field, the latter crosscuts the former.

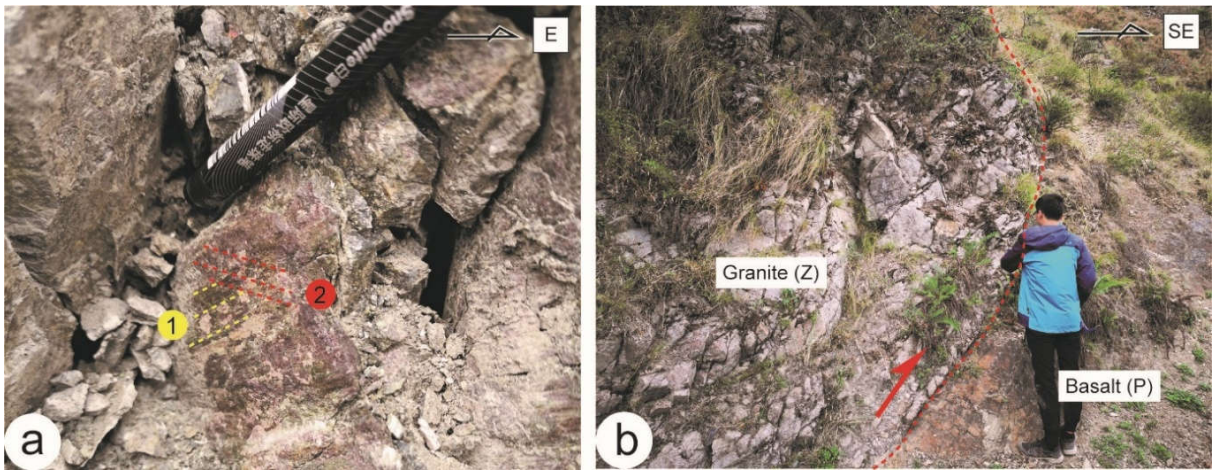

Fig. 8 Field observations around the Mianning area of site CD760. (a) two groups of slickensides on the fault plane. Fault plane striking N20° 80°W with slickensides trending N350° cut by another one trending N215°. (b) Structural contact between Sinian granite and Permian basalt at site CD760.

4 Thermochronological constraints of the JQTB

4.1 Sampling strategy and methods

Complex structures and strong topography affect isotherms in the upper crust which may significantly influence fission track ages (Braun, 2002). To constrain the exhumation rate, it is thus better to sample along vertical transects. We sampled an altitudinal transect (Baishagou transect) in the hanging wall of the Yalong thrust over a relief of ~1000 m and culminating at 2443 m (Figure 2). The horizontal distance of the Baishagou transect is ~ 1.3 km to reduce the topography effect as much as possible. The nine samples were collected in an undeformed granite, the Jurassic Baishagou granite (Figure 2) (Wang et al., 2014). They yielded nine AFT ages (Table 1) and four AHe ages (Table 2). Neither deformation nor faults were detected in-between the samples.

Apatite fission track samples were dated by the LA-ICP-MS method (Gleadow et al., 2015). Apatite grains were set in a regular array in epoxy resin and polished to expose a flat surface for etching. Following this, the AFT grains were etched in 5 N HNO_3 at 21℃ for 20 s to reveal the spontaneous tracks. Sample preparation and spontaneous fission-track counting were performed at the State Key Laboratory of Geological Processes and Mineral Resources, China University of Geosciences, Wuhan, using the Autoscan system. In order to reduce the error due to the low spontaneous track density, we tried to choose the largest grains and count the track

density in the area as wide as possible. The U content was measured by LA-ICP-MS at the State Key Laboratory of Geological Processes and Mineral Resources. NIST 612 glass and 43Ca of apatite were used as an internal standard to correct the U concentrations of apatite aliquots.

AHe analyses were conducted at the University of Arizona, USA. Four good quality, inclusion-free, grains per sample have been used. The selected grains were loaded into Nb tubes and heated with a laser before cryogenic purification. Helium contents were measured using quadrupole mass spectrometry. Subsequently, aliquots were dissolved in dilute HNO3 and the U, Th, and Sm contents have been obtained through ICP-MS (Ehlers & Farley, 2003). Measured ages have been corrected by applying the α-ejection correction (Farley, 2002).

4.2. Pseudo-elevation and age profile

The AFT ages from the Baishagou transect range between 26.9 Ma and 16.7 Ma and show a strong relationship with altitude with all samples below 2198 m being younger than ~18.5 (Figure 9a). All ages were calculated from high-quality grains that have a homogeneous track distribution, lack inclusions, and involved counting as large an area as possible. The χ^2 test of all samples is >5% with low age dispersion, indicating a single age population. The three AHe ages gave similar ages at ~15 Ma. To ensure a better interpretation of the exhumation history, a composite pseudo-elevation and age profile were plotted (Figure 9b, c). The AHe ages were plotted against true elevation, while the AFT ages elevations were increased by a constant value calculated from the closure temperature difference between the AFT and AHe systems (Reiners and Brandon, 2006). Assuming a geothermal gradient of 30 °C/km, a closure temperature of 65 °C and 110 °C for AHe and AFT thermochronometric systems respectively (Wagner and van den Haute, 1992; Farley, 2002) suggests an increase in elevation of 1500 m. The obtained plot can be interpreted in two different ways (Fig 9b and 9c).

(1) A single event model corresponding to one constant Oligocene-Miocene exhumation. The mean exhumation rate calculated by the single least-squares regression slope is ~0.15 km/Myr with a relatively low correlation coefficient (R^2=0.69), and two AFT and two AHe samples outside of the 95% confidence interval (Figure 9b).

(2) A two episode exhumation history, with a break in slope at 2200 m and ~19 Ma. The linear regression of the upper part of the profile corresponds to a very slow exhumation rate of ~0.03 km/Myr (R^2=0.99; Figure 9c), while the lower part shows a relatively rapid exhumation of ~0.31 km/Myr between ~19 and 14 Ma (R^2=0.90) that would correspond to at least 1700 m of exhumation (Figure 9c).

Given the difference in age between the AFT and AHe for a given sample, this can yield estimates of the cooling rate. Assuming that the closure temperature of AFT and AHe system is 65 °C and 110 °C respectively (Wagner and van den Haute, 1992; Farley, 2002), the rates would be ~4 °C/Ma between ~27 and 15 Ma for CD746, ~7°C/Ma between ~22 and 15 Ma for CD747, and ~ 11°C/Ma between ~19 and 14 Ma for CD749. This suggests that the cooling rate significantly increased after 19 Ma. This strongly suggests that the increase in the cooling rate is correlated with the increase in the exhumation rate outlined in the two stages model (Figure 9c) and thus that it reveals an increase in the exhumation rate at ~19 Ma. Furthermore, the two highest samples (CD746 and CD747, Table 1) show shorter track lengths than the other samples (Table 1) indicating that they stayed in the AFT PAZ during the slow cooling phase until ~22 Ma prior to cool rapidly together with the other samples.

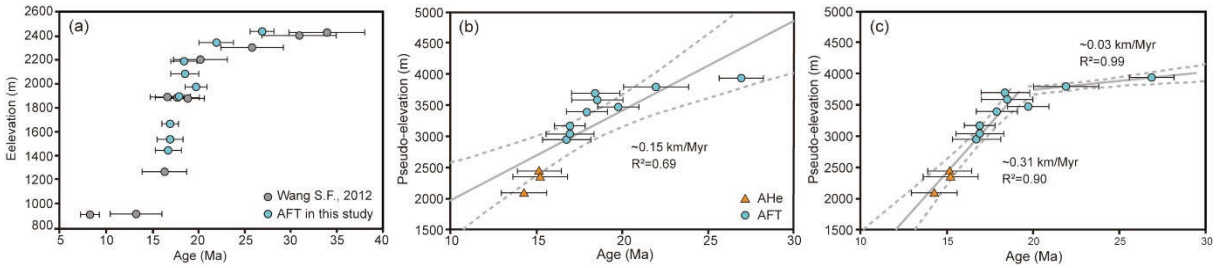

Fig. 9 Pseudo-elevation and age profile of AFT and AHe samples. (a) AFT ages compared to S. Wang, (2012). (b) A single linear regression model with stable exhumation history. (c) Two episode exhumation model, which has a break in slope point at ~19 Ma. The gray solids are the least-squares regression relationships of the samples, and the dashed gray lines represent the 95% confidence intervals.

4.3. Thermal Modeling

To better constrain the cooling and exhumation history of the Baishagou granite, we performed QTQt modeling (Gallagher, 2012) based on the nine AFT ages and three AHe ages. Sample CD753 yielded three AHe grain ages (Table 2), however, two of them are older than the corresponding AFT age (16.9 ± 1.4 Ma), probably because of the bad quality of the apatite grains, and have been discarded. Furthermore, we prefer to not use the third single crystal age whose reproducibility cannot be tested. In this model, prior constraints are as follows: (a) the present-day surface temperature is 10 ± 10 °C; (b) the geothermal gradient is set to ~30 ± 30 °C/km. The temperature offset was permitted to vary over time because of the unstable paleo-geothermal gradient. We did not dispose of any precise and reliable constraints on the temperature-time history of the Baishagou granite and the QTQt models were performed without any external constraint, to avoid overinterpretation of the modeling result (Vermeesch

& Tian, 2014). The modeling results are shown in Figure 10, including the maximum likelihood model and the expected model derived from the QTQt inverse modeling.

The maximum likelihood model corresponds to the model with the lowest misfit with the data (Gallagher, 2017). It reproduces well the AFT and AHe ages and the track length data (Figure 10a, b). This model presents a three-stage cooling history. First ~20 Ma of slow cooling from ~140 to 130 °C at a rate of ~0.5 °C/Myr, second rapid cooling between 20 and 15 Ma at a rate of 10 °C /Myr, and three slow cooling from ~60-40°C at a rate of ~2 °C/Myr (Figure 10a). The timing of initiation of the fast cooling phase at ~20 Ma is similar to the timing of the break-in slope in the pseudo-elevation age profile (Figure 9b). Subsequently, the rocks underwent a faster cooling that we interpreted to have resulted from the rapid exhumation of the rocks. Taking the geothermal gradient calculated from the QTQt model (30 °C/km for the first episode and 26 °C/km for the others), the exhumation rate between 20 and 15 Ma is 0.415 ± 0.075 km/Myr corresponding to ~1.7-2.4 km of total exhumation. After ~15 Ma, a period of slow cooling corresponds to less than ~1 km of exhumation.

The expected model is a weighted mean model that yields a range of possible cooling histories at a 95% range for each parameter and is expected to show smoother cooling histories than the maximum likelihood model (Gallagher, 2017). As a matter of fact, the results show a more progressive transition from slow (~1-2 °C/Myr) to relatively fast cooling (~7-8 °C/Myr) to at about 24-20 Ma, followed by a stage of moderate cooling (~2-3 °C/Myr) after ~15-11 Ma (Figure 10c). The fit between predicted and observed ages in this model is not as good as the maximum likelihood model, even though the results are within the error bars (Figure 10d).

To conclude, both models imply a relatively fast cooling (10 to 7 °C/Myr) between 24-20 and 15-11 Ma, which we interpret as the result of rapid exhumation.

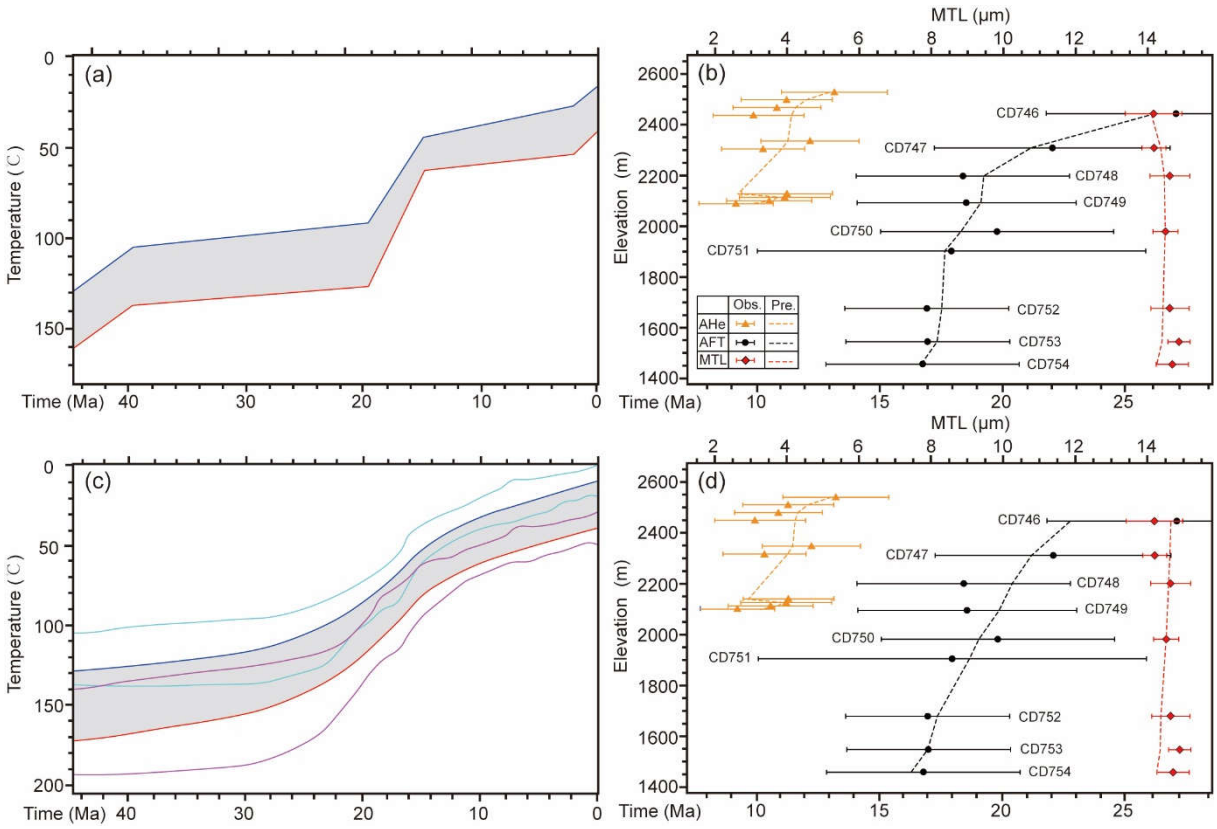

Fig. 10 Cooling history of the Baishagou vertical profile based on QTQt inverse modeling. (a) and (c) Cooling history derived from the maximum likelihood model and the expected model, respectively. (b) and (d) Comparison between the observed and predicted values for all samples in the profile (single-grain ages for AHe and central ages for AFT). For the highest elevation sample, the thermal history is plotted by the blue curve and the 95% credible intervals are drawn in cyan. For the lowest elevation sample, the thermal history is plotted by the red curve and the 95% credible intervals are drawn in magenta. Intermediate sample thermal histories are shown in the grey area. MTL=mean track length

5 Discussion

5.1 Exhumation mechanism(s) of the Baishagou granite

Few published thermochronology studies have focused on the exhumation of the Yalong region of the JQTB (Figure 1). S. Wang et al. (2012) reported a fast exhumation at ~17 Ma derived from AFT samples scattered along a ~80 km horizontal distance in the footwall of the Yalong fault (Figure 2). Upstream along the Yalong river, Clark et al. (2005) reported ~13-9 Ma rapid river incision from samples collected from the upper wall of the Muli thrust fault. Our data imply that the fast cooling of the Baishagou granite occurred between 24-20 and 15-11 Ma. It is more likely that this cooling occurred between 20 and 15 Ma at a rate of 10°C/Ma and corresponds to ~1.7-2.4 km of exhumation at a rate of ~0.4 km/Myr. The granite lies in the deep

Yalong river gorges in the footwall of the Muli thrust and the hanging wall of the Yalong and Nibi faults (Figure 2). Two main processes can be proposed for exhumation: fluvial erosion or uplift in the hanging wall of a thrust fault. However, a more regional uplift mechanism cannot be ruled out. For example, some workers have linked the deep erosion of the Yalong river to lower crustal flow at depth that would have propagated from the Tibetan Plateau towards the southeast during the Late Miocene (~13 Ma) (Clark & Royden, 2000; Clark et al., 2005; Ouimet et al., 2010). As discussed above the timing of exhumation of the Baishagou granite is constrained to start ~20 Ma, which is significantly older than the age proposed for the onset of exhumation linked with lower crustal channel flow in that area (~13 Ma, Clark & Royden, 2000; Clark et al., 2005). This will be discussed in more detail below.

The Anninghe fault is an active left-lateral strike-slip fault that is the southern extension of the Xianshuihe fault system and is located along the Anninghe River 32 km east of the Baishagou granite (Figure. 2). This fault could have played a role in the exhumation of the Yalong area. However, it is a strike-slip fault with a very small vertical component that could probably not have induced the ~2 km exhumation recorded in the Baishagou region. For example, the slickensides observed at site CD760 probably belong to a branch of the Anninghe fault and show very little vertical component (Figure 2). Furthermore, the fault is the prolongation of the Xianshuihe fault, which is considered to be younger than 9 Ma (Zhang et al, 2017), or even possibly ~5 Ma (Wang et al., 2009) at this location.

Alternatively, several faults straddle the Mianning-Yalong zone (Figure 2, Figure 7i) and could have induced the exhumation of the Baishagou granite. The Muli fault is an NW dipping thrust outcropping 12 km to the NW and would thus induce subsidence, not uplift, of the Baishagou granite. Alternatively, the granite lies in the hanging wall of the Yalong and Nibi thrusts (Figure 2, Figure 7i). S. Wang et al. (2012) provided the AFT ages of ten samples from four locations in between the Yalong and Nibi faults (Figure 2). When plotted together with our data, their ages define roughly the same age versus altitude relationship implying a strong common exhumation between ~20 and 15 Ma (Figure 9a). Because all these samples are in the hanging wall of the Nibi fault, it suggests that this fault is responsible for this exhumation. The upper part of the plot, however, possibly shows a ≤7 Ma offset between the two data sets (Figure 9a). Such offset could result from a faster exhumation of the samples west of the Yalong fault until ~20 Ma, which would be compatible with a small reverse motion on the fault at that time. After 20 Ma, both data sets show fast exhumation that we have constrained to be at ~0.4 km/Ma until 15 Ma from the QTQt modeling of our data. Data from S. Wang (2012) suggest that fast exhumation lasted until ~15 Ma and was followed by a slower exhumation phase (Figure 9a),

suggesting that the Nibi fault ceased at that time. A 1300 m elevation difference is observed from the Anning He valley bottom to the ridge in the hanging wall of the Nibi fault. We suggest that most of this difference results from the ~1.7-2.4 km early Miocene fast exhumation in the hanging wall of the Nibi fault.

5.2 Timing of the Jinhe-Qinghe Thrust Belt

As described above, the JQTB runs for more than 300 km from the Yalong-Mianning area to the Xilapin area, bringing Sinian rocks on top of Mesozoic sediments (Figure 2). Our field observations confirm that the JQTB is a thrust with 1 to 4 km of apparent vertical displacement. Locally, the JQTB shows a large left-lateral component, however, the amount of displacement is difficult to estimate. In Tanjiawan, Eocene sediments are found in the footwall of the JQTB implying that the fault is younger than 33.15 ± 0.21 Ma (Figure 4g).

In the Mianning-Yalong zone, the Nibi thrust was active since ~20 Ma. The prolongation of the thrust to the south is not clear. One possibility is that it is a branch of the JQTB (Figure 2) in which case this would constrain the JQTB to have been active between ~20 and ~15 Ma.

5.3 Regional tectonic implications

5.3.1 Compatibility with the channel flow model

One of the processes that have been invoked for the uplift/exhumation of the southeastern Tibet margin is a flow of partially molten lower crust pushed outward from the Tibetan Plateau by body forces due to its exceptional thickness. The flow would be halted and pushed upward by the stiff Sichuan craton to create the LMS range, while it would be continuous across the Yunnan margin inducing a smoother relief. In that model, an uplift wave progressively propagates from west to east, inducing river incision and erosion ((Clark & Royden, 2000; Clark et al., 2005). The Yalong river incision at 13-9 Ma derived from AFT and AHe data was taken as a proxy for river incision and thus the propagation of channel flow across the Yalong margin (Clark et al., 2005; Ouimet et al., 2010).

However, a growing number of studies document erosion/exhumation timings that are not in accord with the channel flow hypothesis, i.e. a simple propagation from west to east through time. For example, surface uplift in the Daocheng took place between ~22 and 15 Ma (Figure. 1) (Tian et al., 2014), whilst other fast exhumation of the hanging wall along the Jiulong thrust fault took place at ~35-30 Ma and between 8 and 7 Ma (Zhang et al., 2016). Near Xiangcheng, the fast exhumation and entrenching of the Shuoqu River (upper reach of the Yangtze River) lasted from 18-15 to 12 Ma (Gourbet et al., 2019). Along the Jiulong River, incision started at

13-9 Ma (Clark et al., 2005), whilst our study located further downstream of the Yalong river and 15 km east, documents exhumation starting at ~20 Ma. Such timing is incompatible with a channel flow model for the entrenching of the Yalong river.

5.3.2 Diachronous Cenozoic exhumation of southeastern Tibet

In the LMS region, two main episodes of rapid exhumation phases during the Cenozoic have been documented. In the central LMS region, these two phases have been dated by low-temperature thermochronology in the Pengguan range at 30-25 to 25-20 Ma (E. Wang et al., 2012) and ~11 Ma to the present day (Godard, 2009; E. Wang et al., 2012). This has been interpreted as two episodes of mountain building, the younger one is still active as shown by the Wenchuan earthquake. In the southwest LMS, the exhumation of the Baoxing granite started prior to 17-15 Ma, while the exhumation in the hanging wall of the Wulong fault started at 12-10 Ma (Cook et al., 2013).

The left-lateral Xianshuihe fault separates the southern LMS from the Yalong thrust (Figure. 1). The total offset has been estimated at ~60 km (e.g., Wang et al., 1998; Wang and Burchfiel, 2000; Yan and Lin, 2015). The timing of onset is disputed, however, Zhang et al. (2017) proposed that it initiated at 12.6 ± 1 Ma in the NW (Wang et al., 2009) and propagated between the LMS and Yalong thrust at ~9 Ma.

Tapponnier et al. (2001) suggested that the thrusts of the Yalong margin correspond to thrusts branching on the Xianshuihe fault during the Eocene-Oligocene. S. Wang et al. (2012) also suggested that the JQTB was a thrust branching of the Xianshuihe fault active at ~17 Ma (Middle Miocene). Our results confirm the timing proposed by S. Wang et al. (2012), however, this hypothesis does not fit with the age of the Xianshuihe fault which is significantly younger in that area (~9 Ma) (Zhang et al., 2017).

To the SW, the JQTB seems to cut the LNF (Figure 2). The LNF thrust is younger than Eocene sediments older than 33.15 ± 0.21 Ma. The LNF trends NNW-SSE almost parallel to the Chenghai and Yulong thrusts. The age of the Yulong thrust has been proposed to be between 28 and 20 Ma (Cao et al., 2019), coeval with E-W compression and left-lateral shear along the Ailao Shan-Red River (ASRR) shear zone (Leloup et al., 1995, 2001, 2007). An age of 28 to 20 Ma for the LNF would be compatible with the age that we propose for the JQTB (20-15 Ma). It thus appears that a single model cannot explain all the exhumation ages now available in southeastern Tibet and that one should envisage several exhumation mechanisms taking place during a multistage history.

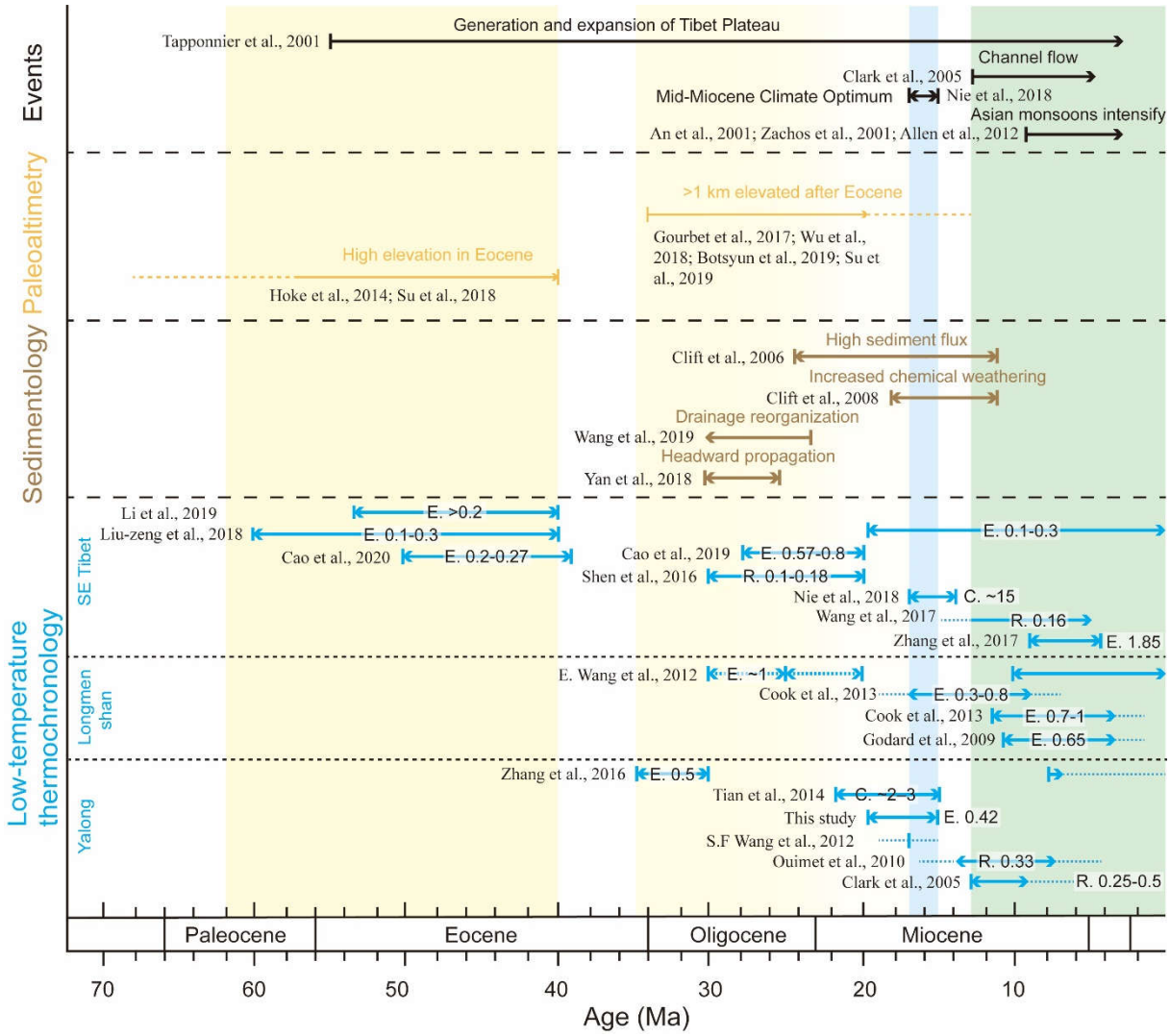

Fig. 11 Regional compilation of fast cooling/exhumation events with respect to paleo-altimetry and sediment flux in the South China Sea. Low-temperature thermochronology studies are derived from age-elevation profiles (see Figure 1 for localization) in southeastern Tibet. E. = exhumation rate, km/Myr; R. =river incision rate, km/Myr; C. =cooling rate, °C/Myr. The yellow zones indicate the uplift events resulting from the southeast extrusion of Tibetan Plateau and its corresponding fast exhumation, sedimentary records and increase in paleo-elevation. The blue rectangle indicates the Mid-Miocene climate optimum. The green rectangle indicates Late Miocene river incision which has been interpreted as due to lower crustal flow.

5.3.3 Multistage history for the growth of relief in the southeastern Tibetan Plateau

The growing data set on the timing of exhumation, including the present study and paleo-altimetry suggest that several mechanisms contributed to the formation of the present-day topography in southeastern Tibet. Below we list several tectonic events that have contributed to the topographic growth of eastern Tibet.

Mesozoic deformation has been widely documented in the eastern Tibet (e.g., Roger et al., 2010), and Cretaceous deformation and metamorphism occurred in the south LMS (e.g., Airaghi et al, 2018) and Danba area (Wallis et al., 2003). These events have probably produced significant relief, however, it is unclear how much of that relief was preserved prior to the Early Eocene at the time of the India-Asia collision. The Jianchuan Eocene basin formed in the footwall of the Ludian-Zhonghejiang thrust that was active between 50 and 39 Ma according to low-temperature thermochronology (Figure 1, Figure 11) (Cao et al., 2020). Such deformation implies NE-SW shortening (in present-day coordinates) (Figure 12) and is comparable to deformation and sedimentation of the HohXil and Yushu-Nangqian basins further west in the Tibetan Plateau (Horton et al., 2002; Spurlin et al., 2005; Staisch et al., 2016). Such deformation produced crustal shortening responsible for significant relief creation. Indeed, some paleo-elevation studies indicate that parts of southeastern Tibet reached high elevation before the Oligocene: Liming basin, 2650 ± 300 m at ≥40 Ma (Hoke et al., 2014), the Jianchuan basin, 2.9 ± 0.6 km at ~36 Ma (Wu et al., 2018), the Gonjo basin, ≥2100-2500 m at ≥43 Ma (Tang et al., 2017), the Markam basin, ~3 km at ~34 Ma (Su et al., 2018). However, studies relying on $\delta^{18}O$ measurements probably overestimated the paleo-elevations (Botsyun et al., 2019). For example, in the Jianchuan basin, the Eocene (~36 Ma) altitude could be re-evaluated to 1200 ± 1200 m depending on the assumptions made for the Eocene conglomerates (Gourbet et al., 2017; Wu et al., 2018). In any case, at least 1 to 2 km of altitude needs to have been gained after the Eocene in western southeastern Tibet and probably much more in the rest of the area.

During the Late Eocene-early Oligocene (35-30 Ma) only one phase of exhumation is documented in eastern Tibet, which is in the hanging wall of the Jiulong thrust (Figure 11, Figure 12a) (Zhang et al., 2017). That time corresponds to a major phase of ultrapotassic magmatism dated between 36.9 and 32.5 Ma. (Schärer et al., 1994; Liang et al., 2007; Chung et al., 2008; Lu et al., 2012). The products of this magmatism is found in a zone with a diameter of ~200 km that was latter cut and offset ~600 km by the left-lateral ASRR (Leloup et al., 2001). A phase of magmatism at ~33 Ma followed by rapid cooling until ~29 Ma in the Xuelong Shan range has been interpreted as being related to the onset of the shear zone (Leloup et al., 2001; Leloup et al., 2007). Gourbet et al. (2017) proposed that doming of the upper crust under the effect of rising magmas due to ultrapotassic magmatism would have been sufficient to provoke a major drainage reorganization. Other studies have linked the ultrapotassic magmatism to lithospheric delamination (Chung et al., 1998, 2005; Lu et al., 2012), in which case it would

have induced a large regional uplift. However, such a hypothesis would require extension, rather than compression, at the time of magmatism.

In the Late Oligocene-Early Miocene (30-20 Ma) (Figure 12b), a major phase of exhumation has been documented interpreted as resulting from a first phase of thrusting along the LMS thrust belt (Figure 11) (E. Wang, 2012), indicating ~NW-SE compression. Contemporaneous exhumation (28-20 Ma) of the Jianchuan basin has been interpreted to be linked to the Yulong thrust fault (Cao et al., 2019) suggesting ~WNW-ESE compression. The Chenghai and LNF thrust most probably activated at the same time. This resulted in the creation or amplification of the relief in the hanging wall of the faults (Figure 12b). As both the Yulong and LMS thrust belts were active at this time, it is tempting to consider that the Muli fault located in between would have also been active. The later activity of that fault is likely based on low-temperature thermochronology (see below), however, the lack of higher temperature thermochronology data precludes any definitive answer.

During 20-15 Ma, the Nibi thrust was active and thus most probably the Jinhe-Qinghe thrust (Figure 12c). Relief creation in the hanging wall of the Jinhe-Qinghe thrust expanded the high Tibetan relief to the southeast. Differential uplift is still visible in the ~1200 m topographic step across the JQTB (Perrineau, 2010; Wu et al., 2019). No significant exhumation has been documented in the central LMS, however, Cook et al. (2013) report a phase of exhumation starting prior to 15 Ma in the Baoxing granite, which is located in the hanging wall of the Erwangmiao fault in the southwestern LMS (Figure 12c). At 15 Ma, all parts of the topographic transition from Tibet to areas of lower elevation had been uplifted and the relief could have been comparable to the present-day relief. Correspondingly, the clastic sediments denudated from southeastern Tibetan Plateau were transported to the South China Sea by large river systems (e.g., Paleo-Red River) and show peaks at ~19 Ma and 17-15 Ma (Clift et al., 2006, 2014), which fits our proposed 20-15 Ma accelerated exhumation very well. The extrusion of Indochina along the ASRR ended at ~17 Ma (Leloup et al., 2001) marking a major tectonic change in the area. One could expect that the Jiulong and Muli thrusts and JQTB would have been activated in that order following the propagation of the Tibetan Plateau toward the southeast, or an in-sequence thrusting from the plateau interior. This is based on the fast exhumation documented at the thrust fault hanging walls of the Jiulong, Muli and Nibi (JQTB) thrusts that show phases of rapid cooling at between ~35 and 30 Ma and between 8 and 7 Ma (Zhang et al., 2016), between ~13 and 5 Ma (Clark et al., 2005) and between 20 and 15 Ma (this study), respectively (Figure 1, Figure 12a-c). Higher temperature thermochronology

system (ZHe and ZFT) focusing on the Muli thrust will provide more information about the earlier exhumation phase of the Muli thrust and its mechanism.

After the end of Indochina extrusion, the left-lateral Xianhuihe fault initiated at ~13 Ma in the northwest (Wang et al., 2009) and propagated to the southeast, reaching the Gongga Shan area at ~9 Ma (Zhang et al., 2017), and further to the southeast probably at ~4 Ma (Figure 12d). The dextral Red River fault initiated along the former ASRR possibly at ~12 Ma (Leloup et al., 2001), or at ~5 Ma (Leloup et al., 1993), when several N-S normal faults re-activated previous thrusts. Between 12 and 8 Ma, several NE-SW thrusts initiated: the Muli fault in the Yalong margin (Pitard et al., submitted), the Wulong fault in the southern LMS (Cook, 2013) and the Beichuan fault in the central LMS (Godard et al., 2009) (Figure 12d). In the two first cases, this implies a late activation of internal faults.

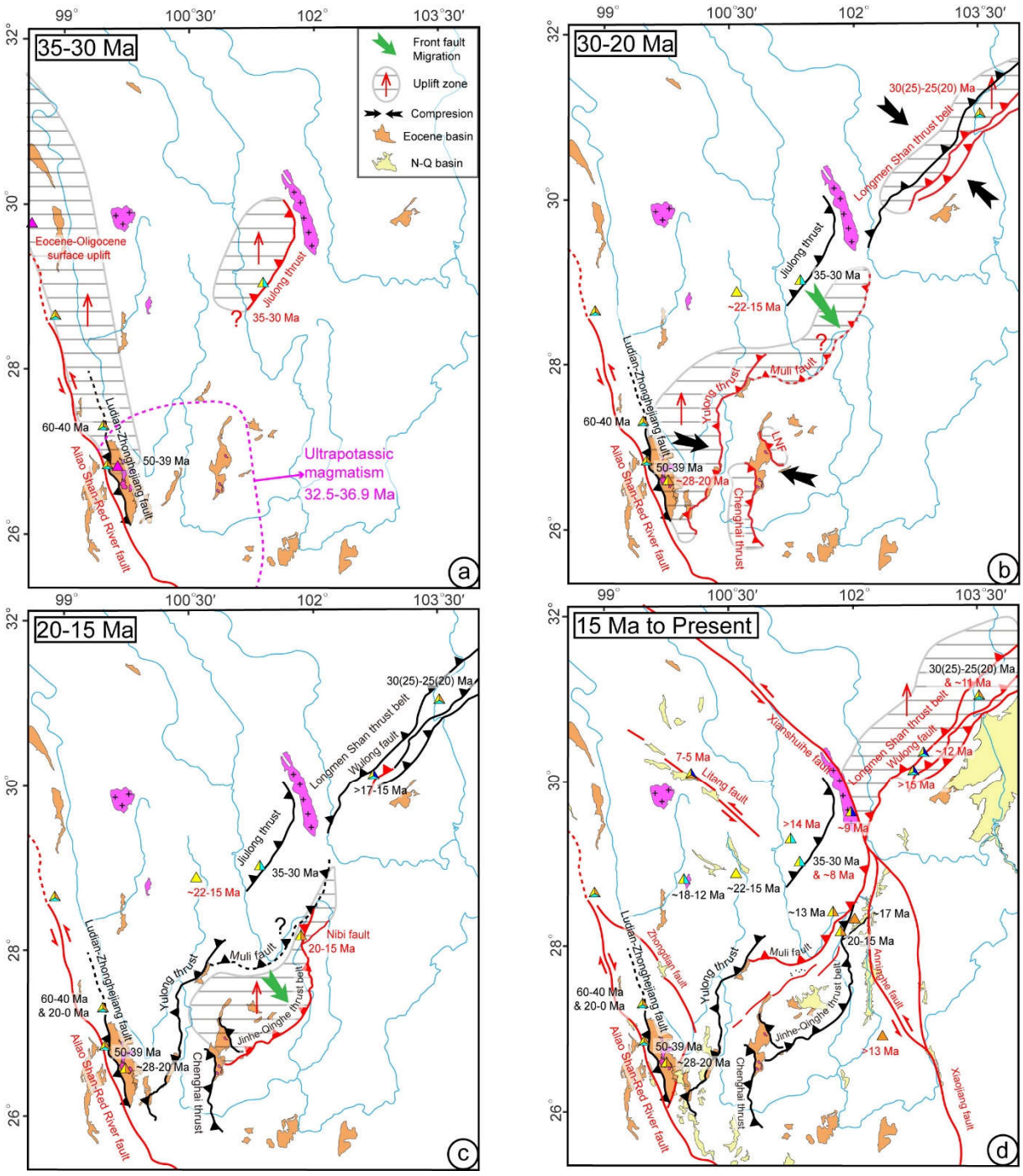

Fig. 12 Late Eocene to present evolution of the southeastern Tibetan Plateau during the southeastward extrusion of Indochina. The differential exhumation resulting from thrusting along thrust belts are responsible for relief generation during the Oligocene to Early Miocene (see details in discussion). N-Q: Neogene-Quaternary.

6. Conclusions

Detailed field observations along the Jinhe-Qinghe thrust belt and low-temperature thermochronology (AFT and AHe dating) from the hanging wall of the Nibi thrust, branch of the JQTB yield new constraints on the amount and timing of thrusting in southeastern Tibet.

The structure analysis shows that the JQTB is a post-Eocene thrust with several branches, with total vertical motion being on the order of ~4.5 km. The pseudo-elevation-age profile and QTQt modeling of the Baishagou granite show that fast exhumation occurred between 20-15 Ma in the hanging wall of the Nibi thrust at a rate of ~0.42 km/Myr corresponding to ~1.7-2.4 km of total exhumation. We consider that the thrusting movement of JQTB is responsible for this rapid exhumation.

When considering previous studies, it appears that Cenozoic exhumation and relief creation in southeastern Tibet does not follow a simple pattern that could be explained by a single mechanism. Based on relict reliefs from previous tectonic events (i.e., Triassic and Cretaceous), at least three stages of Cenozoic shortening and relief creation have to be invoked. The first stage was marked by Eocene NE-SW compression at least partly coeval with the sedimentation of the Eocene sediments. The second stage during the Late Oligocene to Early Miocene corresponds to an NW-SE to E-W compression yielding to thrusting in the LMS, and the Yulong thrust belt. The activity of the JQTB is posterior to that event, corresponding to a southeastern migration of the high plateau through time. A third stage corresponds to the activation of left-lateral strike-slip faults such as the Xianshuihe fault and the re-activation of thrusts such as the Beichuan and Wulong faults in the LMS and the Muli thrust. The precise interaction between thrusting and fast river erosion driven by Miocene monsoon strengthening as documented around 11-8 Myr ago (An et al., 2001; Zachos et al., 2001; Allen et al., 2012) has not been deciphered yet, but Oligocene - Miocene thrusting appears to explain most of the present-day relief in southeastern Tibet.

Acknowledgments

We thank Kerry Gallagher for proving us the new version of modeling software and the guidance of QTQt modeling. We are also grateful to Andrew Gleadow for the helpful suggestions about the fission track dating based on LA-ICP-MS. We also thank editor Taylor Schildgen, for the helpful suggestion that improved the manuscript. This work is funded by the National Science Foundation of China (41672195). All the data documented are listed in the references or archived in Figshare repository (10.6084/m9.figshare.12726941).

REFERENCES

Airaghi, L., de Sigoyer, J., Guillot, S.,Robert, A., Warren, C. J., & Deldicque, D., (2018). The Mesozoic along-strike tectonometamorphic segmentation of Longmen Shan (eastern Tibetan plateau). *Tectonics*, 37. https://doi.org/10.1029/2018TC005005

Allen, C.R., Luo, Z.L., Qian, H, Wen, X.Z., Zhou, H.W., & Huang, W.S., (1991). Field study of a highly active fault zone: the Xianshuihe fault of southwestern China. *Geological Society of America Bulletin*, 103, 1178–1199. https://doi.org/10.1130/0016-7606(1991)103<1178:FSOAHA>2.3.CO;2

Allen, M.B., & Armstrong, H.A., (2012). Reconciling the Intertropical Convergence Zone, Himalayan/Tibetan tectonics, and the onset of the Asian monsoon system. *Journal of Asian Earth Sciences*, 44, 36–47. https://doi.org/10.1016/j.jseaes.2011.04.018

An, Z.S., Kutzbach, J.E., Prell, W.L., & Porter, S.C., (2001). Evolution of Asian monsoons and phased uplift of the Himalaya-Tibetan plateau since late Miocene times. *Nature*, 411, 62–66. https://doi.org/10.1038/35075035

Botsyun, S., Sepulchre, P., Donnadieu, Y., Risi, C., Licht, A., & Rugenstein, J.K.C., (2019). Revised paleoaltimetry data show low Tibetan Plateau elevation during the Eocene. *Science*, 363, 946. https://doi.org/10.1126/science.aaq1436

Braun J., (2002). Quantifying the effect of recent relief changes on age–elevation relationships. *Earth and Planetary Science Letters*, 200(3):331–343. https://doi.org/10.1016/S0012-821X(02)00638-6

Burchfiel, B. C., Chen, Z. L., Liu, Y. P., & Royden, L. H., (1995). Tectonics of the Longmen Shan and adjacent regions, central China. *International Geology Review*, 37(8), 661–735. https://doi.org/10.1080/00206819509465424

Bureau of Geology and Mineral Resources of Sichuan Province (map G47-06, G47-12, G48-01, H47-36, H48-31, scale 1:200,000), (1991). Regional geology of Sichuan Province, Geological Publishing House, Beijing.

Bureau of Geology and Mineral Resources of Yunnan Province (map G47-11, scale 1:200,000), (1990). Regional Geology of Yunnan Province, Geological Publishing House, Beijing.

Cao, K., Wang, G.C., Leloup, P. H., Mahéo, G., Xu, Y.D., van der Beek, P. A., et al., (2019). Oligocene-Early Miocene topographic relief generation of southeastern Tibet triggered by thrusting. *Tectonics*, 38. https://doi.org/10.1029/2017TC004832

Cao, K., Leloup, P.H., Wang, G.C., Liu, W., Mahéo, G., Shen, T.Y., et al., (2020). Thrusting, exhumation, and basin fill on the western margin of the South China block during the India-Asia collision. *Geological Society of America Bulletin*, https://doi.org/10.1130/B35349.1

Chung, S.-L., Lo, C.-H., Lee, T.-Y., Zhang, Y., Xie, Y., Li, X., et al., (1998). Diachronous uplift of the Tibetan plateau starting 40 Myr ago. *Nature*, 394 (6695), 769–773. https://doi.org/10.1038/29511

Chung, S.-L., Chu, M.-F., Zhang, Y., Xie, Y., Lo, C.-H., Lee, T.-Y., & Wang, Y., (2005). Tibetan tectonic evolution inferred from spatial and temporal variations in post-collisional

687 magmatism. *Earth-Science Reviews*, 68 (3–4), 173–196.
688 https://doi.org/10.1016/j.earscirev.2004.05.001
689 Clark, M.K., & Royden, L.H., (2000). Topographic ooze: building the eastern margin of
690 Tibet by lower crustal flow. *Geology*, 28, 703–706. https://doi.org/ 10.1130/0091-
691 7613(2000)28<703:TOBTEM>2.0.CO;2
692 Clark, M.K., House, M.A., Royden, L.H., Whipple, K.X., Burchfiel, B.C., Zhang, X., & Tang,
693 W., (2005). Late Cenozoic uplift of southeastern Tibet. *Geology*, 33, 525–528.
694 https://doi.org/10.1130/G21265.1
695 Clift, P.D., (2006). Controls on the erosion of Cenozoic Asia and the flux of clastic sediment
696 to the ocean. *Earth and Planetary Science Letters*, 241, 571–580. https://doi.org/
697 10.1016/j.epsl.2005.11.028
698 Clift, P.D., Wan, S.M., & Blusztajn, J., (2014). Reconstructing chemical weathering, physical
699 erosion and monsoon intensity since 25 Ma in the northern South China Sea: A review of
700 competing proxies. *Earth-Science Reviews*, 130 (2014) 86–102. https://doi.org/
701 10.1016/j.earscirev.2014.01.002
702 Cook, K. Royden, L., L. H., Burchfiel, B. C., Lee, Y. H., & Tan, X., (2013). Constraints on
703 Cenozoic tectonics in the southwestern Longmen Shan from low-temperature
704 thermochronology, *Lithosphere*, 5(4), 393–406. https://doi.org/ 10.1130/L263.1
705 Ehlers, T.A., (2005). Crustal thermal processes and the interpretation of thermochronometer
706 data. *Rev. Mineral. Geochem*, 58, 315–350. https://doi.org/10.2138/rmg.2005.58.12
707 Farley K.A., (2002). (U–Th)/He dating: Techniques, calibrations, and applications. *Rev*
708 *Mineral Geochem*, 47(1):819–844. https://doi.org/10.2138/rmg.2002.47.18
709 Gallagher, K., (2012). Transdimensional inverse thermal history modeling for quantitative
710 thermochronology. *Journal of Geophysical Research*, 117, B02408. https://doi.org/
711 10.1029/2011JB008825
712 Gallagher, K., (2017). QTQt v 5.6.0 User Guide. 77 pp.
713 Gao, L., Yang, Z.Y., Tong, Y.B., Wang, H., An, C.Z., & Zhang, H.F., (2017). Cenozoic
714 clockwise rotation of the Chuan Dian Fragment, southeastern edge of the Tibetan Plateau:
715 Evidence from a new paleomagnetic study. *Journal of Geodynamics*, 112(2017), 46-57.
716 https://doi.org/10.1016/j.jog.2017.10.001
717 Ge Y.K., Liu-Zeng, J., Zhang J.Y., Wang W., Tian Y.T., Fox M., et al., (2020). Spatio-temporal
718 variation in rock exhumation linked to large-scale shear zones in the southeastern Tibetan
719 Plateau. *Science China Earth Sciences*, 63, 512–532. https://doi.org/10.1007/s11430-019-
720 9567-y
721 Godard, V., Pik, R., Lave, J., Cattin, R., Tibari, B., de Sigoyer, J., Pubellier, M., & Zhu, J.,
722 (2009), Late Cenozoic evolution of the central Longmen Shan, eastern Tibet: Insight from

(U-Th)/He thermochronometry. *Tectonics*, 28, TC5009. https://doi.org/10.1029/2008TC002407

Gourbet, L., Leloup, P. H., Paquette, J.-L., Sorrel, P., Maheo, G., Wang, G.C., et al., (2017). Reappraisal of the Jianchuan Cenozoic basin stratigraphy and its implications on the SE Tibetan plateau evolution. *Tectonophysics*, 700-701, 162–179. https://doi.org/10.1016/j.tecto.2017.02.007

Hoke, G.D., Liu-Zeng, J., Hren, M.T., Wissink, G.K., & Garzione, C.N., (2014). Stable isotopes reveal high southeast Tibetan plateau margin since the Paleogene. *Earth and Planetary Science Letters*, 394, 270–278. https://doi.org/10.1016/j.epsl.2014.03.007

Horton, B.K., Yin, A., Spurlin, M.S., Zhou, J., & Wang, J., (2002), Paleocene–Eocene syncontractional sedimentation in narrow, lacustrine-dominated basins of eastcentral Tibet: *Geological Society of America Bulletin*, 114 (7), 771–786. https://doi.org/10.1130/0016-7606(2002)114<0771:PESSIN>2.0.CO;2

Hu X.M., Garzanti, E., Wang, J.G., Huang, W.T., An, W., & Webb, A., (2016). The timing of India-Asia collision onset – Facts, theories, controversies. *Earth-Science Reviews*, 160, 264-299. https://doi.org/10.1016/j.earscirev.2016.07.014

Kirby, E., Reiners, P. W., Krol, M. A., Whipple, K. X., Hodges, K. V., Farley, K. A., & Chen, Z., (2002). Late Cenozoic evolution of the eastern margin of the Tibetan Plateau: Inferences from 40Ar/39Ar and (U–Th)/He thermochronology. *Tectonics*, 21, 1001. https://doi.org/10.1029/2000TC001246

Leloup, P. H., Lacassin, R., Tapponnier, P., Scharer, U., Zhong, D.L., Liu, X.H., et al., (1995). The Ailao Shan-Red River shear zone (Yunnan, China), Tertiary transform boundary of Indochina. *Tectonophysics*, 251(1–4), 3–84. https://doi.org/10.1016/0040-1951(95)00070-4

Leloup, P.H., Arnaud, N., Lacassin, R., Kienast, J., Harrison, T., Trong, T.T.P., et al., (2001). New constraints on the structure, thermochronology, and timing of the Ailao Shan-Red River shear zone, SE Asia. *Journal of Geophysical Research*., 106, 6683–6732. https://doi.org/10.1029/2000JB900322

Leloup, P. H., Tapponnier, P., & Lacassin, R., (2007). Discussion on the role of the Red River shear zone, Yunnan and Vietnam, in the continental extrusion of SE Asia. *Journal of the Geological Society*, London, Vol. 164, 2007, pp. 1253–1260. https://doi.org/10.1144/0016-76492007-065

Li, S.Y., Currie, B.S., Rowley, D.B., & Ingalls, M., (2015). Cenozoic paleoaltimetry of the SE margin of the Tibetan plateau: constraints on the tectonic evolution of the region. *Earth and Planetary Science Letters*, 432, 415–424. https://doi.org/10.1016/j.epsl.2015.09.044

Liang, H.Y., Campbell, I.H., Allen, C.M., Sun, W.D., Yu, H.X., Xie, Y.W., & Zhang, Y.-Q., (2007). The age of the potassic alkaline igneous rocks along the Ailao Shan-Red River shear zone: implications for the onset age of left-lateral shearing. *The Journal of Geology*, 115, 231–242. https://doi.org/10.1086/527459

762 Lin, T. H., Lo, C. H., Chung, S. L., Hsu, F. J., Yeh, M. W., Lee, T. Y., et al., (2009). 40Ar/39Ar
763 dating of the Jiali and Gaoligong shear zones: Implications for crustal deformation around
764 the eastern Himalayan syntaxis. *Journal of Asian Earth Sciences*, 34(5), 674–685.
765 https://doi.org/10.1016/j.jseaes.2008.10.009
766 Liu-Zeng, J., Tapponnier, J.P., Gaudemer, Y., & Ding, L., (2008). Quantifying landscape
767 differences across the Tibetan plateau: implications for topographic relief evolution.
768 *Journal of Geophysical Research*, 113, F04018. https://doi.org/10.1029/2007JF000897
769 Liu-Zeng, J., Zhang, J.Y., McPhillips, D., Reiners, P., Wang, W., Pik, R., et al., (2018). Multiple
770 episodes of fast exhumation since Cretaceous in southeast Tibet, revealed by low-
771 temperature thermochronology. *Earth and Planetary Science Letters*, 490, 62–76.
772 https://doi.org/10.1016/j.epsl.2018.03.011
773 Lu, Y. J., Kerrich, R., Cawood, P. A., McCuaig, T. C., Hart, C. J. R., Li, Z. X., et al. (2012).
774 Zircon SHRIMP U-Pb geochronology of potassic felsic intrusions in western Yunnan, SW
775 China: Constraints on the relationship of magmatism to the Jinsha suture. *Gondwana*
776 *Research,* 22(2), 737–747. https://doi.org/10.1016/j.gr.2011.11.016
777 Molnar, P., & Tapponnier, P., (1975). Cenozoic tectonics of Asia: effects of a continental
778 collision. *Science*, 189, 419–426. https://doi.org/ 10.1126/science.189.4201.419
779 Nie, J., Ruetenik, G., Gallagher, K., Hoke, G., Garzione, C. N., Wang, W., et al. (2018). Rapid
780 incision of the Mekong River in the middle Miocene linked to monsoonal precipitation.
781 Nature Geoscience, 11(12), 944–948. https://doi.org/10.1038/s41561-018-0244-z
782 Ouimet, W., Whipple, K., Royden, L., Reiners, P., Hodges, K., & Pringle, M., (2010). Regional
783 incision of the eastern margin of the Tibetan plateau. *Lithosphere*, 2, 50.
784 https://doi.org/10.1130/L57.1
785 Perrineau, A., (2010). Evolution morphologique et tectonique récente des marges NE et SE du
786 plateau tibétain: Lien avec la dynamique des grands fleuves. Institut de Physique du Globe
787 de Paris. 421pp.
788 Reiners, P. W., & Brandon, M. T., (2006). Using thermochronology to understand orogenic
789 erosion. *Annual Review of Earth and Planetary Sciences*, 34(1), 419–466.
790 https://doi.org/10.1146/annurev.earth.34.031405.125202
791 Replumaz, A., Lacassin, R., Tapponnier, P., & Leloup, P. H., (2001). Large river offsets and
792 Plio-Quaternary dextral slip rate on the Red River fault (Yunnan, China). *Journal of*
793 *Geophysical Research*, 106(B1), 819–836. https://doi.org/10.1029/2000JB900135
794 Roger, F., J. Malavieille, P. H. Leloup, S. Calassou, & Z. Xu, (2004). Timing of granite
795 emplacement and cooling in the Songpan-Garze Fold Belt (eastern Tibetan Plateau) with
796 tectonic implications. *Journal of Asian Earth Sciences*, 22(5), 465–481.
797 https://doi.org/10.1016/S0137-9120(03)00089-0
798 Roger, F., Jolivet, M. & Malavieille, J., (2010). The tectonic evolution of the Songpan Garzeˆ
799 (North Tibet). *Journal of Asian Earth Sciences*, 39, 254–269.
800 https://doi.org/10.1016/j.crte.2007.10.014

Royden, L. H., Burchfiel, B. C., King, R. W., Wang, E., Zhiliang, C., Feng, S., & Yuping, L., (1997). Surface deformation and lower crustal flow in eastern Tibet. *Science*, 276(5313), 788–790. https://doi.org/10.1126/science.276.5313.788

Schärer, U., Zhang, L. S., & Tapponnier, P. (1994). Duration of strike-slip movements in large shear zones: The Red River belt, China. *Earth and Planetary Science Letters*, 126(4), 379–397. https://doi.org/10.1016/0012-821X(94)90119-8

Schoenbohm, L.M., Burchfiel, B.C., & Chen, L., (2006). Propagation of surface uplift, lower crustal flow, and Cenozoic tectonics of the southeast margin of the Tibetan plateau. *Geology*, 34, 813–816. https://doi.org/10.1130/G22679.1

Shen, X.M., Tian, Y.T., Li, D.W., Qin, S.W., Vermeesch, P., & Schwanethal, J., (2016). Oligocene-Early Miocene river incision near the first bend of the Yangze River: Insights from apatite (U-Th-Sm)/He thermochronology. *Tectonophysics*, 687, 223–231. https://doi.org/10.1016/j.tecto.2016.08.006

Si, G., Li, Y., & Hou, Z., (2000), The Tertiary stratigraphy sequence of Yanyuan Basin in the southeastern margin of the Qinghai-Tibet Plateau, *Earth Science Frontiers*, 7, 304–305.

Spurlin, M.S., Yin, A., Horton, B.K., Zhou, J., & Wang, J., (2005), Structural evolution of the Yushu-Nangqian region and its relationship to syncollisional igneous activity, east-central Tibet. *Geological Society of America Bulletin*, 117 (9–10), 1293–1317. https://doi.org/10.1130/B25572.1

Staisch, L.M., Niemi, N.A., Clark, M.K., & Chang, H., (2016), Eocene to late Oligocene history of crustal shortening within the Hoh Xil Basin and implications for the uplift history of the northern Tibetan Plateau. *Tectonics*, 35 (4), 862–895. https://doi.org/10.1002/2015TC003972

Su, T., Spicer, R.A., Li, S.H., Xu, H., Huang, J., Sherlock, S., Huang, Y.J., Li, S.F. et al., (2018). Uplift, climate and biotic changes at the Eocene–Oligocene transition in south-eastern Tibet. *National Science Review*, 6(3), 495–504. https://doi.org/10.1093/nsr/nwy062

Tang, M.Y., Liu-Zeng, J., Hoke, G. D., Xu, Q., Wang, W.T., Li, Z.F., et al., (2017). Paleoelevation reconstruction of the Paleocene-Eocene Gonjo basin, SE-central Tibet. *Tectonophysics*, 712-713, 170–181. https://doi.org/10.1016/j.tecto.2017.05.018

Tapponnier, P., Zhiqin, X., Roger, F., Meyer, B., Arnaud, N., Wittlinger, G., & Jingsui, Y., (2001). Oblique stepwise rise and growth of the Tibet plateau. *Science*, 294(5547), 1671–1677. https://doi.org/10.1126/science.105978

Tian, Y.T., Kohn, B.P., Gleadow, A.J., & Hu, S.B., (2013). Constructing the Longmen Shan eastern Tibetan plateau margin: insights from low-temperature thermochronology. *Tectonics*, 32, 576–592. https://doi.org/10.1002/tect.20043

Tian, Y.T., Kohn, B.P., Gleadow, A.J.W., & Hu, S.B., (2014). A thermochronological perspective on the morphotectonic evolution of the southeastern Tibetan plateau. *Journal of Geophysical Research*, 119, 676–698. https://doi.org/10.1002/2013JB010429

Vermeesch, P., & Tian, Y. T., (2014). Thermal history modelling: HeFTy vs. QTQt. *Eart-Science Reviews*, 139, 279–290. https://doi.org/10.1016/j.earscirev.2014.09.010

841 Wallis, S., Tsujimori, T., Aoya, M., Kawakami, T., Terada, T., Suzuki, K., & Hyodo, H., (2003).
842 Cenozoic and Mesozoic metamorphism in the Longmenshan orogen: Implications for
843 geodynamic models of eastern Tibet. *Geology*, 31 (9): 745–748.
844 https://doi.org/10.1130/G19562.1
845 Wang, E., Burchfiel, B.C., Royden, L.H., Chen, L., Chen, J., Li, W., & Chen, Z., (1998). The
846 Cenozoic Xianshuihe–Xiaojiang, Red River, and Dali Fault Systems of southwestern
847 Sichuan and central Yunnan, China. Spec. Pap., *Geological Society of America Bulletin*,
848 327. 108 https://doi.org/10.1130/0-8137-2327-2.1
849 Wang, E., & Burchfiel, B.C., (2000). Late Cenozoic to Holocene deformation in southwestern
850 Sichuan and adjacent Yunnan, China, and its role in formation of the southeastern part of
851 the Tibetan Plateau. *Geological Society of America Bulletin*, 112, 413–423.
852 https://doi.org/10.1130/0016-7606(2000)112<413:LCTHDI>2.0.CO;2
853 Wang, E., Kirby, E., Furlong, K., van Soest, M., Xu, G., Shi, X., Kamp, P., & Hodges, K.,
854 (2012). Two-phase growth of high topography in eastern Tibet during the Cenozoic.
855 *Nature. Geoscience*, 5, 640–645. https://doi.org/10.1038/ngeo1538
856 Wang, G.C., Zhang, K.X., Xiang, S.Y., Wang, A., Cao, K. et al., (2014). Cenozoic geological
857 map and guidebook of Tibet Plateau and its adjacent regions 1:1 500 000, 2014. China
858 University of Geosciences Press. Wuhan, p 155.
859 Wang, H., Tian, Y., & Liang, M., (2017). Late Cenozoic exhumation history of the Luoji Shan
860 in the southeastern Tibetan Plateau: Insights from apatite fission-track thermochronology.
861 *Journal of the Geological Society*, 174, 883-891. https://doi.org/10.1144/jgs2017-005
862 Wang, S.F., Fang, X.M., Zheng, D.W., & Wang, E., (2009). Initiation of slip along the
863 Xianshuihe fault zone, eastern Tibet, constrained by K/Ar and fission-track ages.
864 *International Geology Review*, 51(12), 1121–1131.
865 https://doi.org/10.1080/00206810902945132
866 Wang, S.F., Jiang, G.G., Xu, T.D., Tian, Y.T., Zheng, D.W., & Fang, X.M., (2012). The Jinhe-
867 Qinghe fault—An inactive branch of the Xianshuihe-Xiaojiang fault zone, eastern Tibet.
868 *Tectonophysics*, 544-545, 93–102. https://doi.org/ 10.1016/j.tecto.2012.04.004
869 Wagner G., & van den Haute P., (1992). Fission-track dating. Enke, Stuttgart, p 285.
870 Wu G.L., Zhu C.Y., Wang G.C., & Zhang P., (2019). Demarcation of the geomorphological
871 boundaries of southeastern Tibet: implications for expansion mechanisms of the plateau
872 edge. *Seismology and Geology*, 2(41), 281-299 (in Chinese with English abstract).
873 Wu, J., Zhang, K., Xu, Y., Wang, G., Garzione, C. N., Eiler, J., Leloup, P. H., et al., (2018),
874 Paleoelevations in the Jianchuan Basin of the southeastern Tibetan Plateau based on stable
875 isotope and pollen grain analyses. *Palaeogeography, Palaeoclimatology, Palaeoecology*,
876 510, 93-108. https://doi.org/10.1016/j.palaeo.2018.03.030
877 Xu, G., & Kamp, P. J. J., (2000). Tectonics and denudation adjacent to the Xianshuihe fault,
878 eastern Tibetan plateau: Constraints from fission track thermochronology. *Journal of*
879 *Geophysical Research*, 105(B8), 19,231–19,251. https://doi.org/10.1029/2000JB900159

Yan, B., & Lin, A., (2015). Systematic deflection and offset of the Yangtze River drainage system along the strike-slip Ganzi–Yushu–Xianshuihe fault zone, Tibetan Plateau. *Journal of Geodynamics*, 87, 13–25. http://doi/10.1016/j.jog.2015.03.002

Yang, R., Fellin, M.G., Herman, F., Willett, S.D., Wang, W., & Maden, C., (2016). Spatial and temporal pattern of erosion in the three rivers region, southeastern Tibet. *Earth and Planetary Science Letters*, 433, 10–20. https://doi.org/10.1016/j.epsl.2015.10.032

Zachos, J., Pagani, M., Sloan, L., Thomas, E., & Billups, K., (2001). Trends, rhythms, and aberrations in global climate 65 Ma to present. *Science*, 292, 686–693. https://doi.org/10.1126/science.1059412

Zhang, B., Zhang, J.J., Chang, Z.F., Wang, X.X., Cai, F.L., & Lai, Q.Z., (2012). The Biluoxueshan transpressive deformation zone monitored by synkinematic plutons, around the eastern Himalayan syntaxis. *Tectonophysics*, 574-575, 158–180. https://doi.org/10.1016/j.tecto.2012.08.017

Zhang, H.P., Oskin, M. E., Liu-Zeng, J., Zhang, P.Z., Reiners, P. W., & Xiao, P., (2016). Pulsed exhumation of interior eastern Tibet: Implications for relief generation mechanisms and the origin of high-elevation planation surfaces. *Earth and Planetary Science Letters*, 449, 176–185. https://doi.org/10.1016/j.epsl.2016.05.048

Zhang, P. Z., Shen, Z., Wang, M., Gan, W. J., Burgmann, R., Molnar, P., et al., (2004). Continuous deformation of the Tibetan Plateau from global positioning system data. *Geology*, 32(9), 809–812. https://doi.org/10.1130/G20554.1

Zhang, Y. Z., Replumaz, A., Wang, G. C., Leloup, P. H., Gautheron, C., Bernet, M., et al., (2015). Timing and rate of exhumation along the Litang fault system, implication for fault reorganization in southeast Tibet. *Tectonics*, 34, 1219–1243. https://doi.org/10.1002/2014TC003671

Zhang, Y. Z., Replumaz, A., Leloup, P. H., Wang, G. C., Bernet, M., van der Beek, P., et al., (2017). Cooling history of the Gongga batholith: Implications for the Xianshuihe fault and Miocene kinematics of SE Tibet. *Earth and Planetary Science Letters*, 465, 1–15. https://doi.org/10.1016/j.epsl.2017.02.025

Table 1. Apatite fission track ages

Sample No.	Longitude (°E)	Latitude (°N)	Elevation (m)	Grains (*N*)	ρ_s ($10^6 cm^{-2}$)	Ns	U* (ppm)	P(χ^2) (%)	Dispersion (%)	Pooled Age (Ma±1σ) (%)	MTL±1σ (μm) (*N*)	Dpar (μm)
CD746	101.8693	28.3298	2443	24	2.595	116	7.8	41.09	0	26.9±1.3	13.49±1.13 (9)	1.87
CD747	101.8723	28.3273	2351	25	2.283	91	8.6	50.24	0	21.9±1.9	13.48±0.51 (9)	1.75
CD748	101.8759	28.3273	2198	24	2.878	80	9.6	44.05	0	18.4±1.4	13.88±1.10 (11)	1.85
CD749	101.8773	28.3272	2093	22	2.079	75	9.5	42.59	5	18.5±1.5	NA	1.99
CD750	101.8781	28.3291	1980	23	2.238	75	9.4	38.66	0	19.7±1.2	13.62±0.78 (12)	NA
CD751	101.8803	28.3293	1903	5	1.314	22	29.2	22.84	0	17.9±1.2	NA	NA
CD752	101.8772	28.3335	1676	24	2.209	112	10.1	55.95	0	16.9±0.9	13.85±0.81 (7)	1.84
CD753	101.8774	28.3354	1545	24	2.106	115	9.6	42.94	0	16.9±1.4	13.89±0.53 (7)	2.02
CD754	101.8795	28.3364	1455	22	1.700	79	9.1	51.38	0	16.7±1.4	13.84±1.07 (14)	1.85

Note: *N*=Number of grains dated and Number of track length measured; ρs = spontaneous fission-track density; *Ns* = total number of spontaneous fission tracks counted; U*=Mean uranium content of all crystals measured by LA-ICP-MS; P(χ2) = chi-squared probability can represent a single population of ages for υ where degrees of freedom υ= N−1; MTL = Mean confined track length

Table 2 Apatite (U-Th)/He Result From the Baishagou Vertical Profile

Sample	Grain replicate	Mass (μg)	Radius (μm)	U (ppm)	Th (ppm)	Sm (ppm)	eU (ppm)	Th/ U	4He (nmol/g)	FT 238U	FT 235U	FT 232Th	Raw Age (Ma)	Corrected age (Ma)	1σ (Ma)
CD746	Ap1	3.80	57.02	10.42	38.86	143.33	23.38	3.82	1.17	0.749	0.714	0.714	10.94	**14.91**	0.18
	Ap2	5.15	72.39	10.16	34.53	146.33	13.94	3.49	1.32	0.799	0.771	0.771	13.25	**16.82**	0.19
	Ap3	3.24	61.54	9.97	35.60	139.28	11.29	3.66	1.15	0.766	0.734	0.734	11.43	**15.19**	0.18
	Ap4	3.03	56.27	9.35	33.42	130.69	13.88	3.67	0.94	0.746	0.711	0.711	10.03	**13.72**	0.18
CD747	Ap2	1.88	45.5	11.39	28.88	236.97	11.99	2.60	1.23	0.762	0.730	0.730	12.29	**16.34**	0.18
	Ap3	1.19	37.7	11.03	56.56	214.46	15.61	5.26	1.39	0.757	0.724	0.724	10.43	**14.09**	0.16
CD749	Ap1	1.2	39.4	10.53	54.04	184.63	17.47	5.26	1.19	0.754	0.720	0.720	9.35	**12.69**	0.15
	Ap2	2.33	44.5	11.96	52.62	191.00	16.23	4.51	1.50	0.787	0.758	0.758	11.27	**14.57**	0.15
	Ap3	2.14	45.9	10.12	54.82	203.96	16.80	5.56	1.34	0.779	0.749	0.749	10.64	**13.94**	0.15
	Ap4	1.17	37.3	10.47	51.85	170.42	19.97	5.08	1.41	0.735	0.699	0.699	11.38	**15.88**	0.17
CD753	*Ap1*	*1.11*	*35.9*	*10.52*	*37.56*	*171.00*	*16.02*	*3.66*	*2.11*	*0.751*	*0.717*	*0.717*	*19.88*	***26.98***	*0.28*
	Ap3	0.87	34	9.76	34.42	158.62	15.15	3.62	0.85	0.784	0.753	0.753	8.71	**11.29**	0.12
	Ap4	*1.62*	*43.2*	*10.01*	*34.65*	*155.87*	*15.55*	*3.55*	*1.44*	*0.747*	*0.712*	*0.712*	*14.54*	***19.84***	*0.20*

The AHe ages substantially exceed corresponding AFT ages are seemed outliers and not used for weighted mean age calculation and inverse modeling.

915